

# Orthogonal Light-Dependent Membrane Adhesion Induces Social Self-Sorting and Member-Specific DNA Communication in Synthetic Cell Communities

Ali Heidari,\* Oya I. Sentürk,\* Shuo Yang,\* Alex Joesaar,\* Pierangelo Gobbo,\* Stephen Mann,\* Tom F. A. deGreef,\* and Seraphine V. Wegner\*


Developing orthogonal chemical communication pathways in diverse synthetic cell communities is a considerable challenge due to the increased crosstalk and interference associated with large numbers of different types of sender-receiver pairs. Herein, the authors control which sender-receiver pairs communicate in a three-membered community of synthetic cells through red and blue light illumination. Semipermeable protein-polymer-based synthetic cells (proteinosomes) with complementary membrane-attached protein adhesion communicate through single-stranded DNA oligomers and synergistically process biochemical information within a community consisting of one sender and two different receiver populations. Different pairs of red and blue light-responsive protein-protein interactions act as membrane adhesion mediators between the sender and receivers such that they self-assemble and socially self-sort into different multicellular structures under red and blue light. Consequently, distinct sender-receiver pairs come into the signaling range depending on the light illumination and are able to communicate specifically without activation of the other receiver population. Overall, this work shows how photoswitchable membrane adhesion gives rise to different self-sorting protocell patterns that mediate member-specific DNA-based communication in ternary populations of synthetic cells and provides a step towards the design of orthogonal chemical communication networks in diverse communities of synthetic cells.

## 1. Introduction

Intercellular communication is essential to coordinate the collective operation of individual cells and to establish multicellular structures with specialized cells.<sup>[1,2]</sup> For this, sender cells secrete signals in the form of diffusible chemicals which can be recognized by receiver cells within the signaling range and with appropriate receptors. Building similar capabilities into synthetic cells allows community-based functions and interactions among synthetic cells<sup>[3,4]</sup> and living cells.<sup>[5]</sup> Remarkable achievements of communication in synthetic cells include communities that process DNA-coded information through reaction networks,<sup>[6]</sup> mimic quorum sensing,<sup>[7,8]</sup> differentiate into different patterns,<sup>[9]</sup> exhibit prey-predatory relationships,<sup>[10]</sup> synchronization,<sup>[11]</sup> and oscillations,<sup>[12,13]</sup> and regulate cellular behavior in response to physiological conditions.<sup>[14]</sup> These studies illustrated how communication in synthetic cells helps to understand underlying organizational

A. Heidari, S. V. Wegner  
Institute of Physiological Chemistry and Pathobiochemistry  
University of Münster  
Waldeyerstr. 15, 48149 Münster, Germany  
E-mail: heidaria@uni-muenster.de; wegnerse@exchange.wvu.de

O. I. Sentürk  
Department of Physical Chemistry of Polymers  
Max Planck Institute for Polymer Research  
Ackermannweg 10, 55128 Mainz, Germany  
E-mail: sentuerk@mpip-mainz.mpg.de

 The ORCID identification number(s) for the author(s) of this article can be found under <https://doi.org/10.1002/smll.202206474>.

© 2023 The Authors. Small published by Wiley-VCH GmbH. This is an open access article under the terms of the Creative Commons Attribution License, which permits use, distribution and reproduction in any medium, provided the original work is properly cited.

DOI: 10.1002/smll.202206474

S. Yang, A. Joesaar, T. F. A. Greef  
Laboratory of Chemical Biology and Institute for Complex Molecular Systems  
Department of Biomedical Engineering  
Eindhoven University of Technology  
Eindhoven 5612 AZ, The Netherlands  
E-mail: yangshuo19870414@gmail.com; A.H.Joesaar@tudelft.nl; t.f.a.d.greef@tue.nl

P. Gobbo  
Department of Chemical and Pharmaceutical Sciences  
University of Trieste  
Trieste 34127, Italy  
E-mail: pierangelo.gobbo@units.it

S. Mann  
Centre for Protolife Research and Centre for Organized Matter Chemistry  
Max Planck Bristol Centre for Minimal Biology  
School of Chemistry  
University of Bristol  
Bristol BS8 1TS, UK  
E-mail: s.mann@bristol.ac.uk

principles, program multicellular communities towards new applications, and interface synthetic cells with living ones.<sup>[15,16]</sup>

Communication between synthetic cells depends on the spatiotemporal distribution of the signaling molecule, which is affected by the local densities of sender and receiver cells and the production, release, propagation, degradation, and consumption rates of the signal.<sup>[17]</sup> In synthetic sender cells with a limited signal reservoir, the signaling range is limited to the direct neighborhood after which the signal is diluted below its effective concentrations.<sup>[4]</sup> Consequently, the spatial organization of the sender and receiver is critical for the perception of the signal.<sup>[18,19]</sup> Prominent examples of such short-range communication in biology include the neurotransmitters that signal within the neural network and different immune cells that adhere to each other for effective exchange.<sup>[20,21]</sup> In synthetic cell communities, senders and receivers can be placed within signaling range with microfluidic techniques,<sup>[22]</sup> acoustic waves,<sup>[23]</sup> or optical tweezers.<sup>[24]</sup> In addition, the direct adhesions between synthetic cells give rise to the self-assembly of large multiprotocellular structures and regulate signal exchange in bulk solution.<sup>[25,26]</sup>

The number of different cell types is an important characteristic of a community to consider as the number of possible binary relationships increases rapidly with the increasing number of cell types ( $[n^2 - n]/2$ ). Therefore, in diverse synthetic cell communities, the specificity of communication between different pairs becomes a concern and this is why most studies are limited to two-membered communities. Biology has solved the problem of specificity through the spatial distribution of senders and receivers in short-range paracrine signaling, which provides a principle that can also be implemented with synthetic cells.<sup>[25]</sup> When more than two different types of cell-sized microscale objects (e.g., colloids) are mixed, multiple possibilities of spatial arrangement are conceivable along with different self-sorting patterns that arise from the specificity of the surface interactions. In mixtures, specific homophilic adhesions between colloids result in narcissistic self-sorting, where each member of the community forms its own sub-assemblies.<sup>[27,28]</sup> In contrast, specific heterophilic interactions result in social self-sorting, where domains with two member types emerge but other populations are excluded.<sup>[28,29]</sup> Following similar principles different cell types are sorted into different cell layers during early embryonic development.<sup>[30]</sup>

The self-assembly and self-sorting of dispersed synthetic cells require specific and non-interfering (orthogonal) interactions between different populations in response to distinct stimuli. Here, we demonstrate how social self-sorting and communication can be dynamically regulated in a three-membered community of synthetic cells. The community is composed of one sender and two potential receivers and can be socially self-sorted into different structures under either red or blue light. Depending on the illumination conditions, a different receiver cell comes into the signaling range of the sender protocell and perceives the liberated chemical signal. Towards this goal, we use two pairs of light-dependent heterophilic protein-protein interactions to induce selective adhesions and social self-sorting of semipermeable protein-polymer-based synthetic cells (proteinosomes).<sup>[31]</sup> The protein-protein interactions are triggered with different colors of light, determined by

photo-induced conformational changes that open up specific binding sites for the cognate binding partner. In this paper, we employ red light for the binding of the proteins PhyB and PIF6,<sup>[32]</sup> and blue light for the binding of the proteins iLID and Nano.<sup>[33]</sup> In each case, protein binding requires only low intensities of light and is accomplished in buffered solutions. Given these properties, we couple the light-responsive proteins to the outer surface of different proteinosomes to produce a community of synthetic cells with complementary membrane-attached adhesion mediators that when initiated results in self-sorting and define chemical communication. We employ a signaling pathway based on a previously reported DNA-based protocell programming network (biomolecular implementation of protocellular communication, BIO-PC), where different proteinosomes communicate through distributed DNA strand displacement (DSD) reactions.<sup>[17,22]</sup> DSD cascade reactions are highly programmable and utilizing sequence-specific DNA gates can code for functions such as oscillations,<sup>[34]</sup> digital logic circuits,<sup>[35,36]</sup> and Boolean neural networks.<sup>[37]</sup> Taken together, our work exemplifies, how the multicolor light regulation of organization in three-membered communities of synthetic cells dictates the outcome of chemical communication.

## 2. Results

To functionalize the proteinosome membrane with photo-switchable proteins capable of acting as adhesion mediators, we prepared proteinosomes decorated with Ni<sup>2+</sup>-NTA (nitrilotriacetic acid) so that proteins with a polyhistidine tag (His-tag) could be immobilized on the outer surface of the synthetic cells. The proteinosomes were prepared by adapting a previously reported three-step protocol.<sup>[31]</sup> In short, protein-polymer conjugates were synthesized by reacting the primary amines of cationized bovine serum albumin (BSA-NH<sub>2</sub>, labeled with Rhodamine B for fluorescence microscopy visualization of the proteinosomes) with the mercaptothiazoline-activated terminal amide of poly *N*-isopropyl acrylamide (PNIPAM). In addition, 1% of the PNIPAM sidechains contained NTA functionalities (PNIPAM-co-NTA) (Scheme S1, and Figures S1–S9, Supporting Information, characterization through <sup>1</sup>H and <sup>13</sup>C NMR, FT-IR and MALDI spectroscopy, determination of LCST, zeta potential and hydrodynamic diameter). Subsequently, the proteinosomes were formed by the interfacial assembly of the protein-polymer conjugates at the water droplet/oil interface of a Pickering emulsion. The conjugates were then cross-linked and the proteinosomes were transferred to the water phase (Figure S10, Supporting Information). The NTA groups on the resultant proteinosomes were subsequently loaded with Ni<sup>2+</sup> ions. To demonstrate that the Ni<sup>2+</sup>-NTA groups on the surface are accessible, we incubated the proteinosomes with the His-tagged fluorescent protein, miCy. We observed bright miCy fluorescence for proteinosomes with Ni<sup>2+</sup>-loaded NTA groups but control proteinosomes that were not loaded with Ni<sup>2+</sup> were not fluorescent (Figure S11, Supporting Information). The surface density of His-tagged proteins on the proteinosomes was  $\Gamma = 4949 \mu\text{m}^{-2}$  (Figure S11D,E, Supporting Information), which was determined by comparing the fluorescence intensity from His-tagged GFP on the periphery of proteinosomes and

giant unilamellar vesicles with 1% Ni<sup>2+</sup>-NTA containing lipids known lipid packing.<sup>[38]</sup> In addition, we determined in ssDNA uptake measurements that functionalization with His-tagged proteins did not change the membrane permeability of the proteinosomes (Figure S12, Supporting Information). The results indicated that the binding of His-tags to Ni<sup>2+</sup>-NTA groups is a reliable method for attaching auxiliary proteins to the outer surface of the proteinosome membrane; thus, in all subsequent experiments, the proteinosomes were functionalized with the desired His-tagged proteins.

To control the self-assembly of two-membered communities of proteinosomes with adhesions that are triggered independently using different colors of light, we co-functionalized potential sender (S) proteinosomes with PhyB and iLID proteins and two prospective receiver proteinosomes with either PIF6 (R1) or Nano (R2). When we mixed equal numbers of S and R1 proteinosomes, the two types adhered to each other under red light but not in the dark or under blue light illumination (Figure 1A). On the other hand, mixtures of the S and R2 proteinosomes only aggregated under blue light and not in the dark or under red light illumination (Figure 1B). The adhesions between the S and R proteinosomes led to membrane deformations and large contact sides (Figures S13 and S14, Supporting Information). Moreover, we quantified the aggregation ratio (area of objects larger than 2000 μm<sup>2</sup>/area of all objects) of these proteinosome mixtures after 90 min shaking on a 2D shaker at 30 rpm with different illumination conditions. (Appropriate shaking was important to increase the likelihood of the proteinosomes coming into contact; however, too high

shear forces can also disrupt the aggregates).<sup>[39]</sup> For the S:R1 mixture, the proteinosome aggregation ratio was about four times higher under red light illumination than under dark or blue light illumination (Figure 1C). Similarly, for the S:R2 mixture the aggregation ratio was two-fold higher under blue light than in the dark or under red light. As proteinosomes have a broad size distribution (diameter = 10–70 μm, median = 20 μm, area = 79–3850 μm<sup>2</sup>, median = 314 μm<sup>2</sup>) (Figure S15, Supporting Information), the aggregation ratio only takes into account large clusters (>2000 μm<sup>2</sup>) to avoid counting large single proteinosomes. Consequently, this method disregards clusters composed of multiple small proteinosomes. Despite underestimating the aggregation ratio, the extent of proteinosome aggregation was above 50% for S:R1 and S:R2 mixtures under red and blue light, respectively. Overall, the results showed that membrane-bounded photoswitchable protein pairs PhyB/PIF6 and iLID/Nano are suitable to induce the contact-dependent adhesion of proteinosomes when exposed to specific wavelengths of light.

To illustrate how the communication in synthetic cells can be modulated through the light-controlled proximity of S and R proteinosomes, we distributed different steps of the DSD cascade reaction between the two populations.<sup>[22]</sup> In our design, the S-type proteinosomes contained a DNA gate complex F1Q1, where the biotinylated F1 strand was labeled with an Alexa488 fluorophore (1.3 μM) and anchored to a streptavidin (15 μM) (Figures S16 and S17, Supporting Information), and the Q1 strand acted as a fluorescence quencher when hybridized with F1 (Figure 2A). The R-type proteinosomes were loaded with

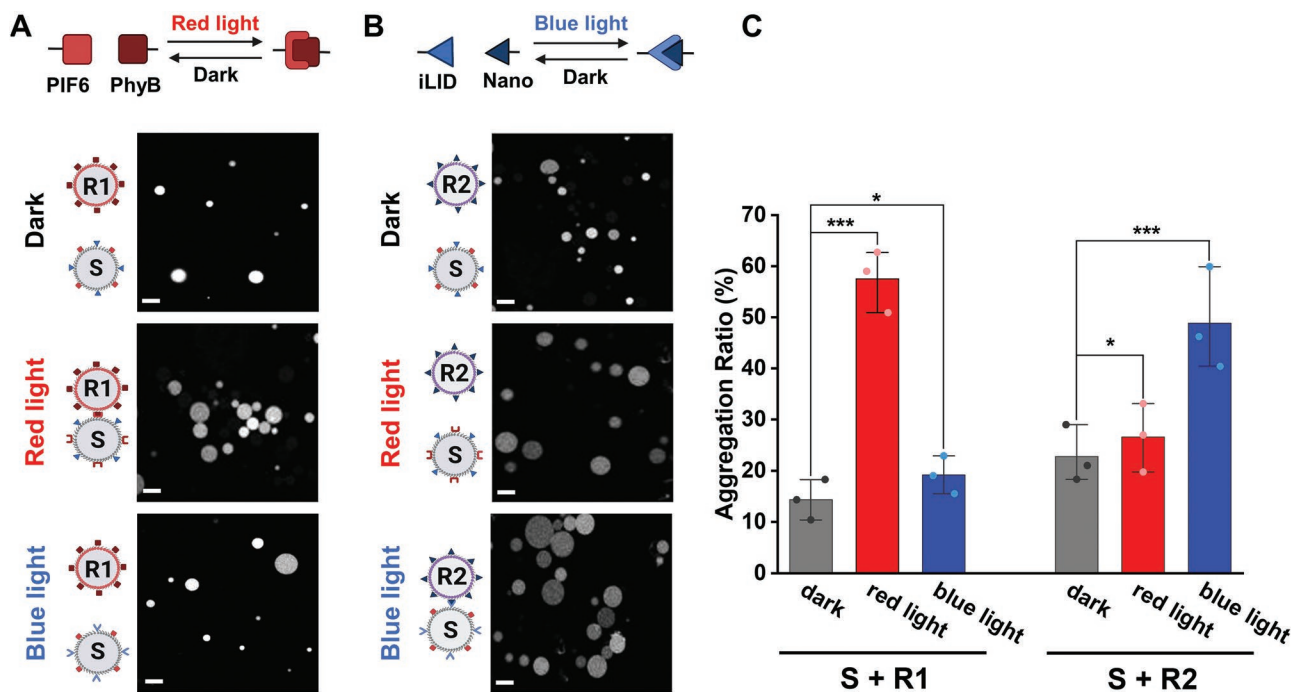


**Figure 1.** Red or blue light controlled aggregation in two membered proteinosome communities. Fluorescence confocal microscopy images of S proteinosomes functionalized with PhyB and iLID and mixed with A) PIF6 functionalized R1 proteinosomes or B) Nano functionalized R2 proteinosomes in the dark, under red light or under blue light after 90 min incubation. S and R1 aggregate under red light due to the red light-triggered binding of PhyB and PIF6. S and R2 adhere to each other under blue light due to the blue light-dependent binding of iLID and Nano. Scale bars are 30 μm. C) Aggregation ratio of S:R1 and S:R2 proteinosome mixtures under different conditions. Error bars are the standard error of the mean from three independent experiments with > 50 proteinosomes per sample.

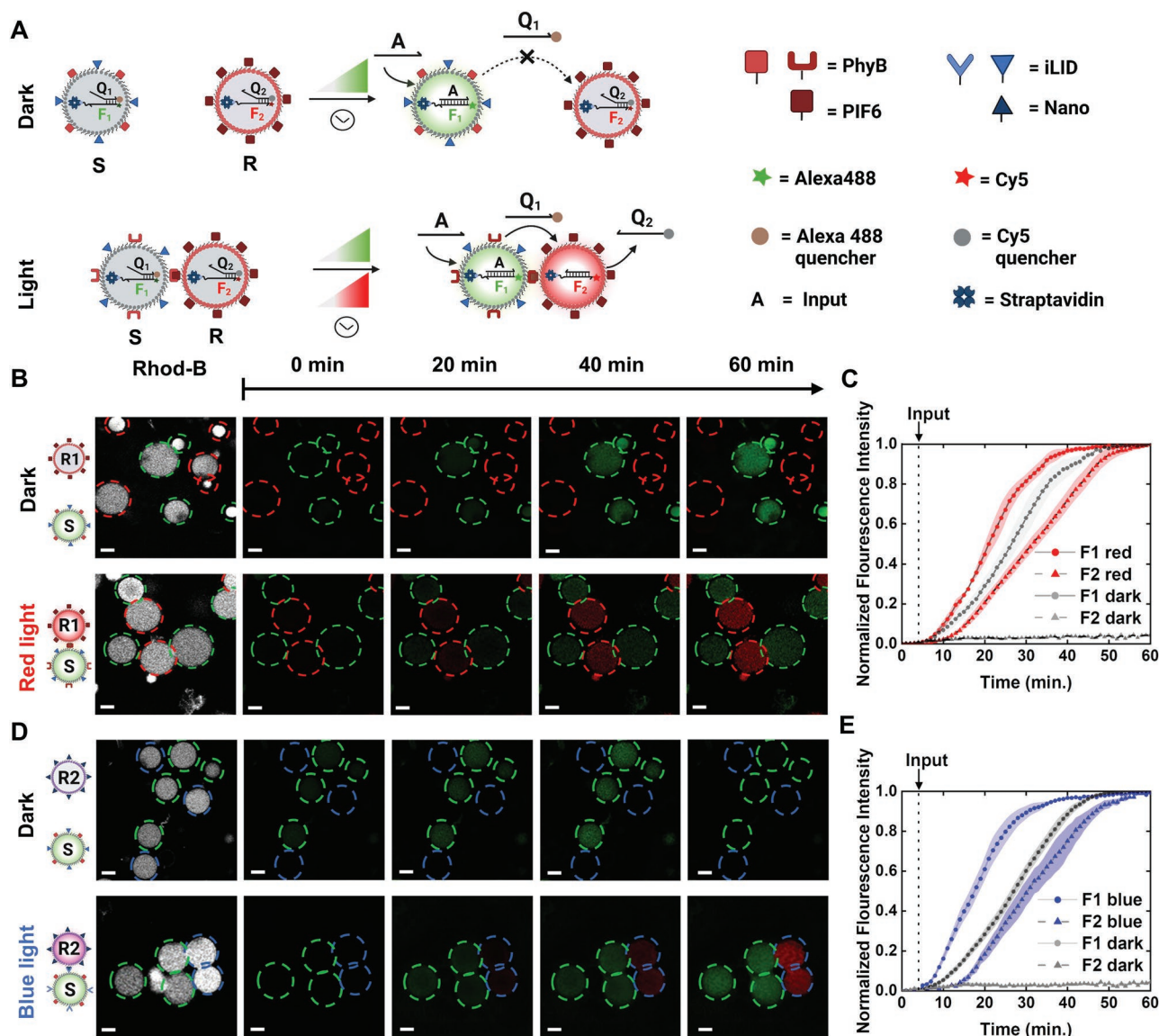


**Figure 2.** Light-regulated proximity controls communication between sender and receiver proteinosomes. A) S-type proteinosomes loaded with F1Q1 DNA gate complex release Q1 and exhibit an increase in Alexa488 green fluorescence upon the addition of the input strand A in the first step of the DSD cascade. In the dark, R-type proteinosomes are too far from S-type proteinosomes and do not receive the Q1 signal. Under the light of appropriate wavelength, S- and R-type proteinosomes are in close proximity, and Q1 displaces the Q2 strand from the F2Q2 DNA gate complex, resulting in an increase in Cy5 red fluorescence. B, D) Confocal microscopy images recorded in Rhod-2 (white), Alexa488 (green), and Cy5 (red) channels of S (circled in green) with R1 (circled in red) or R2 (circled in blue) proteinosomes (S:R ratio 1:1) in the dark and under red or blue light illumination, respectively, after 90 min prior incubation. Strand A is then added at  $t = 0$  min. The scale bars are 20  $\mu\text{m}$ . C, E) Normalized fluorescence intensity of Alexa488 in S (F1 strand) and Cy5 on R (F2 strand) proteinosomes. The fluorescence of individual proteinosomes ( $n > 45$ ) in three independent experiments was measured and the error bars are the standard error of the mean.

an F2Q2 DNA gate complex, where the streptavidin-anchored F2 strand was labeled with Cy5 and Q2 with a corresponding quencher. The DSD reaction cascade was designed such that in the first step the addition of an ssDNA input strand (A) displaces Q1 from the F1Q1 complex, resulting in an increase in Alexa488 fluorescence in S and the concomitant release of Q1 as a diffusive chemical signal. In the second step, if the Q1 signal reaches an R proteinosome, displacement of the Q2 strand from the F2Q2 complex gives rise to an increase in Cy5 fluorescence in R. Notably, given that the S proteinosomes can

only release a limited amount of signal (Q1 strand), only R type proteinosomes in their direct neighborhood where the local signal is high enough can respond. The release profile of the Q1 strand from the S proteinosomes with different sizes (diameter, 30–70  $\mu\text{m}$ ), showed that at a distance of 5  $\mu\text{m}$  from the membrane the concentrations diluted to the background level (Figure S18, Supporting Information), which corresponds to a signaling range below the average size of a proteinosome.

To demonstrate how the proximity of sender and receiver proteinosomes regulates the selective chemical communication

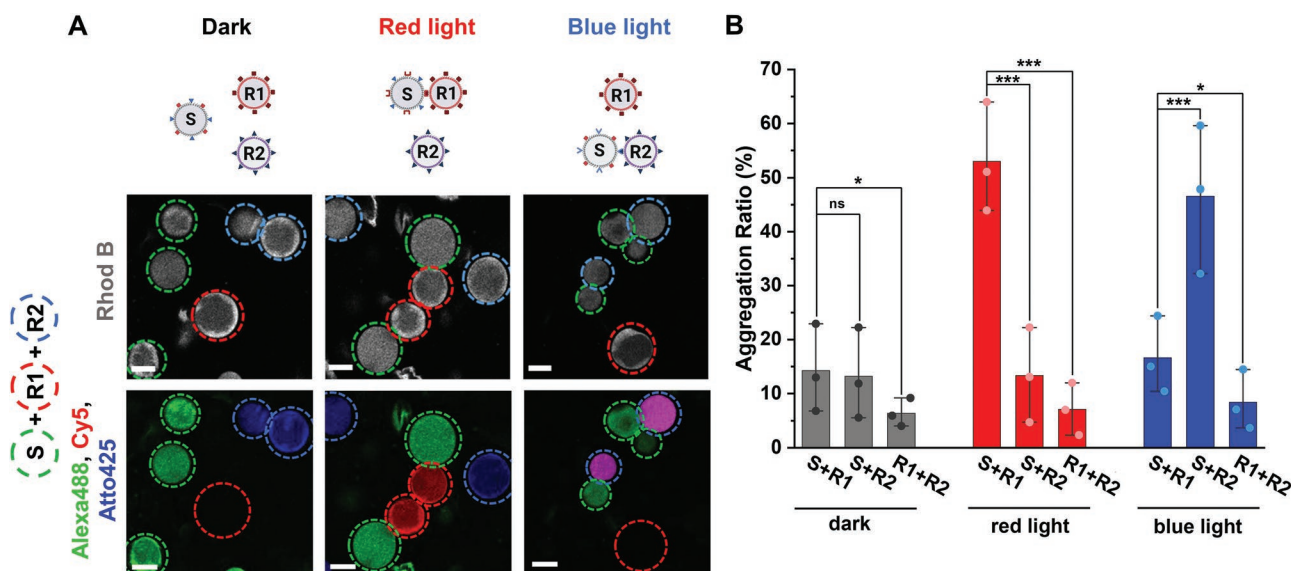


**Figure 3.** Orthogonal social self-sorting with red and blue light in three-membered synthetic cell communities. A) Confocal microscopy images of S, R1, and R2 proteinosomes (2:1:1 ratio) after 90 min incubation under different illumination conditions. While all proteinosomes remain dispersed in the dark, S and R1 adhere under red light due to membrane PhyB-PIF6 binding; in contrast, S and R2 adhere under blue light due to iLID-Nano binding. The scale bars are 20  $\mu\text{m}$ . B) Aggregation ratio between different pairs in the three-membered communities under different illumination conditions. Error bars are the standard error of the mean from three independent experiments with > 100 proteinosomes per sample.

between synthetic cells, we controlled the average inter-protocell spacing through photoswitchable adhesions (Figure 2A). For this, equal numbers of S- and R- type proteinosomes were mixed and incubated for 90 min either in the dark or under red (S:R1) or blue (S:R2) light (Figure 2B,D). In illuminated samples, the S and R populations formed clusters but remained dispersed in the dark. Subsequent addition of the input strand A to the bulk solution initiated the first step of the DSD cascade, which was visible as an increase in Alexa488 green fluorescence inside the S-type proteinosomes. The increase in fluorescence took place in the dark and under light illumination. In contrast, the second step of the DSD cascade, as evidenced by an increase in Cy5 fluorescence in the R-type proteinosomes, only took place under red light illumination in S:R1 and under blue light illumination in S:R2 populations. The population-level quantification of the two DSD reactions over time in the two-membered communities showed that for the first step of the DSD reaction, the increase in Alexa488 fluorescence reached a maximum over time both in the dark and under light, which shows the finite capacity of S to produce the soluble signal (Figure 2C,E). In addition, the Cy5 output of the second DSD reaction emerged with a time delay compared to the Alexa488 signal in the illuminated samples (Figure 2C,E), confirming the sequence of events in the communication pathway. Overall, the results show that molecular communication between the proteinosomes depends on the spatial connectivity of the proteinosomes, which can be tuned with red or blue light illumination.

Given the above observations, we sought to demonstrate light-directed social self-sorting behavior as a mechanism for regulating the chemical communication pathways in three-membered synthetic cell communities composed of one sender and two receiver populations. To achieve this, we mixed S-, R1-, and R2-type proteinosomes in a 2:1:1 ratio and analyzed their

self-sorting under different illumination conditions (Figure 3A). As above, the proteinosomes were membrane-functionalized with the respective proteins (S: PhyB and iLID, R1:PIF6, and R2:Nano) and housed the components of the DSD cascade reaction (F1Q1 in S, F2Q2 in R1 and F2Q2 in R2). The R2-type proteinosomes also contained an additional Atto425-biotin label to distinguish between the R1 and R2 populations. In the dark, the three types of proteinosomes remained dispersed in the solution. Under red light, the S and R1 type proteinosomes adhered selectively due to membrane-based PhyB-PIF6 interactions, while the R2 type proteinosomes remained separated. In contrast, under blue light, the S and R2 proteinosomes bound to each other due to the iLID-Nano interactions and the R1 type proteinosomes remained detached. We further analyzed the aggregation ratios of different pairs to confirm orthogonal social self-sorting in the three-membered community (Figure 3B). In the dark, none of the paired interactions, S:R1, S:R2, and R1:R2 showed significant aggregation ratios. In contrast, high aggregation ratios were observed for either the S:R1 or S:R2 pairs after exposure to red or blue light, respectively. Moreover, the constantly low aggregation ratio of the R1:R2 pair independent of the illumination condition and the low S:R1 and S:R2 aggregation under blue and red light, respectively, indicated the low extent of non-specific interactions between the receiver proteinosomes. Taken together, the results indicate that the social self-sorting of S:R1 and S:R2 pairs in three-membered communities can be triggered independently from each other without interference.

Having established selective sorting behavior, we sought to regulate the specificity of the communication pathway through the photo-triggering of spatial organization in three-membered synthetic communities. For this, we added the input ssDNA strand to the ternary population described above and observed

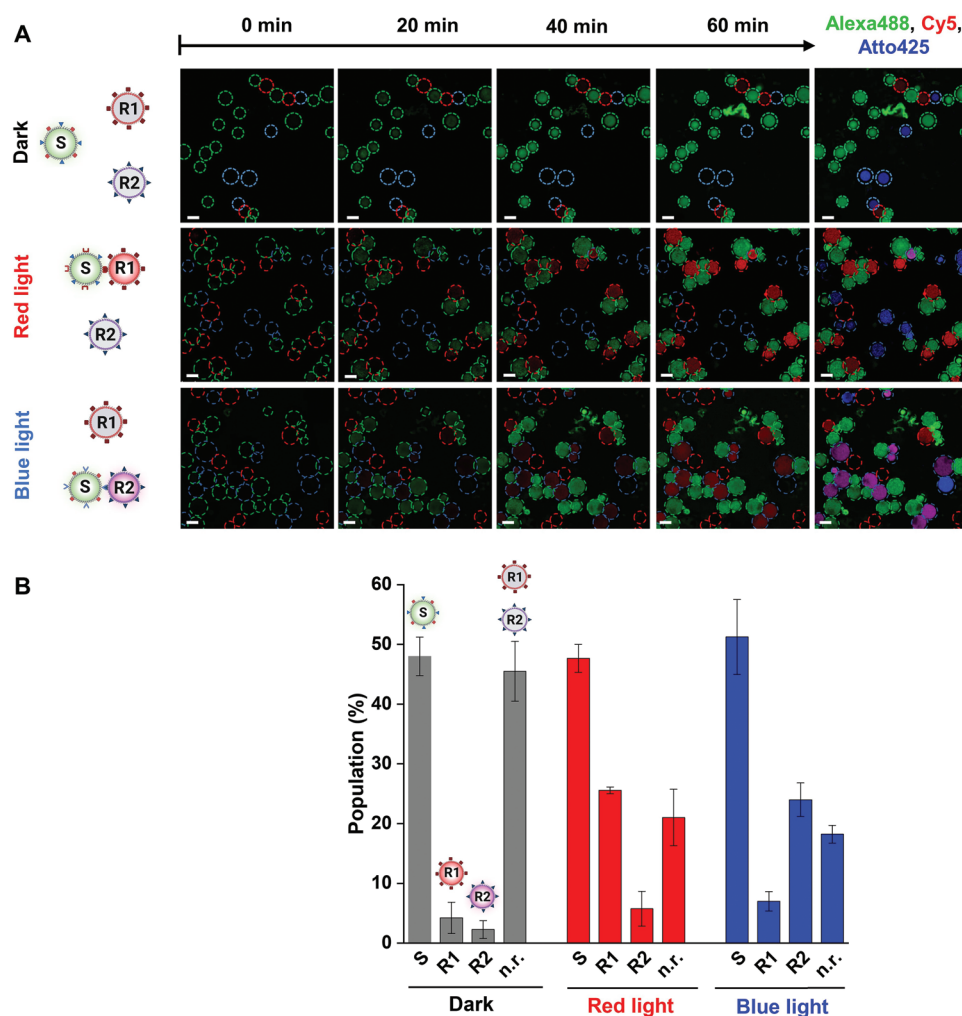


**Figure 4.** Specific DNA-based communication through different social sorting patterns in three-membered proteinosome communities. A) Confocal microscopy images of mixtures of S, R1, and R2 type proteinosomes (2:1:1 ratio) in the dark and under red or blue light illumination, respectively, after 90 min prior incubation. The ssDNA input strand, A, was added at  $t = 0$  min. Alexa488 (green, release of signal strand), Cy5 (red, release of output strand), and Atto425 (blue, identification label) were used to identify S (circled in green), R1 (circled in red), and R2 (circled in blue). While essentially all S proteinosomes increased in Alexa488 fluorescence, only R1 and R2 increased in Cy5 fluorescence under red and blue light, respectively. Purple coloration in R2 proteinosomes is due to the overlay of Cy5 and Atto425 fluorescence. Non-responders were identified from fluorescence images recorded in the rhodamine B (proteinosome membrane label) channel. The scale bars are 50  $\mu\text{m}$ . B) Bar chart showing population percentage of S, activated R1, activated R2, and non-responders (n.r.) under different conditions in (B). Error bars are the standard error of the mean from three independent experiments with  $>50$  proteinosomes per sample.

that the S-type proteinosomes increased in Alexa488 green fluorescence due to the release of the Q1 strand in the first step of the DSD cascade (Figure 4A). In the dark, the proteinosomes remained dispersed and the levels of released Q1 strand were unfunctional due to dilution in the bulk phase; thus, no increase in Cy5 red fluorescence was detected in the R1 or R2 type proteinosomes (Figure 4A). On the other hand, under red light illumination, the Q1 strand reached the attached R1 type proteinosomes, resulting in an increase in Cy5 red fluorescence and indicating successful signal transfer and release of strand Q2 from the R1 (Figure 4A). Conversely, under blue light illumination, Cy5 red fluorescence increased in the R2 population (Figure 4A). To demonstrate that the lack of response in R1 or R2 type proteinosomes was due to the limited local concentrations of Q1 strand released from the S-type proteinosomes and

not due to a lack of functionality in the receivers, we added an external excess of Q1 to the community in the dark and observed that both R1 and R2 type proteinosomes increased in Cy5 fluorescence, confirming their latent activity (Figure S19, Supporting Information).

We quantified the communication response in the three-membered community under different illumination conditions (Figure 4B). Under all conditions (dark, red light, and blue light), the presence of Alexa488 green fluorescence was associated with  $\approx 50\%$  of the total population, consistent with the activation of essentially all the S-type proteinosomes in a community prepared with an initial S:R1:R2 mixing ratio of 2:1:1. In the dark, about 50% of the population were non-responders (no Cy5 output), with less than 5% of the R1 and R2 displaying an increase in Cy5 fluorescence, indicating a low level of

non-specific communication in the absence of light-mediated membrane-membrane adhesions. Under red light, the number of non-responders decreased to 20% and the number of activated R2-type proteinosomes remained at around 5%, but the number of activated R1-type proteinosomes increased to 25%. On the other hand, under blue light, the number of activated R1-type proteinosomes remained at ≈5% but the number of activated R2-type proteinosomes increased to 25%. Taken together, these results demonstrate that the distinct social self-sorting patterns of the different sender and receiver pairs under red and blue light lead to different specific communication outcomes.

### 3. Conclusion

In this paper, we demonstrated that specific communication pathways between different pairs of synthetic cells in mixed communities can be established through the spatial organization of different protocell types as long as the signaling range of the sender population is limited to nearest-neighbor interactions.<sup>[40]</sup> Different modes of self-sorting have been described for colloidal particles<sup>[27,28]</sup> and living cells<sup>[41]</sup> in the context of forming multicellular structures. Here, we show that the social self-sorting of proteinosome-based synthetic cells via selective membrane adhesion events can regulate DNA-based communication in a three-membered community. In particular, our results demonstrate that orthogonal self-sorting and independent photoswitchable triggering can be achieved using the high binding and light specificity of PhyB/PIF6 and iLID/Nano protein pairs. By preparing sender (S) proteinosomes with membranes decorated with both PhyB and iLID “receptors” different patterns of social self-sorting are achieved in the presence of receivers R1 (PIF6) and R2 (Nano) depending on the wavelength of light (red or blue, respectively) used to initiate sender-receiver membrane adhesion. Consequently, S to R1 or S to R2 communication pathways are established in the protocell community using a programmable DSD cascade in which the ssDNA diffusive signal released from S after activation is spatially limited. The orthogonality is maintained as long as the signaling range is restricted to distances below the dimension of a single protocell such that only directly adhered receivers are activated. This short-range effect is facilitated by turbulent mixing in the bulk solution, such that the ssDNA signal is only locally high enough to initiate a response close to its production site and becomes quickly diluted below a critical concentration at longer length scales. This is unlike previous studies using microfluidic chambers with the laminar flow or without any internal flow, where the sender-to-receiver signal only propagates by molecular diffusion. Thus, in contrast to other investigations, our approach offers high spatiotemporal control over the communication process in bulk solutions, without the need for immobilization of the protocells in hydrogels, fabricated chips, or microfluidic arrays.<sup>[22,42–44]</sup> In the long term, we expect the social self-sorting and highly programmable DSD-based communication pathways developed using our methodology to open up possibilities for the advent of diverse and interactive multi-protocellular communities and signaling networks.

### Supporting Information

Supporting Information is available from the Wiley Online Library or from the author.

### Acknowledgements

This work was funded by the European Research Council through the ERC Starting Grant ARTIST (#757593) and ERC Consolidator Grant AMIGA (#101000199). The authors thank Wilfried Weber and Maximilian Hörner from the University of Freiburg for providing the PhyB protein and Brian Kuhlman for the plasmids pQE-80L iLID (C530M) and pQE-80L MBP-SspB Nano (Addgene # 60408 and #60409).

### Conflict of Interest

The authors declare no conflict of interest.

### Data Availability Statement

The data that support the findings of this study are available from the corresponding author upon reasonable request.

### Keywords

DNA-based communication, photoswitchable proteins, proteinosome, self-sorting, synthetic cells

Received: October 20, 2022

Revised: December 3, 2022

Published online:

- [1] J. T. Bonner, *Integr. Biol.* **1998**, *1*, 27.
- [2] R. J. Wordinger, T. Sharma, A. F. Clark, *J. Ocul. Pharmacol. Ther.* **2014**, *30*, 154.
- [3] J. M. Smith, R. Chowdhry, M. J. Booth, *Front. Mol. Biosci.* **2022**, *8*, 809945.
- [4] L. Aufinger, F. C. Simmel, *Chem. – Eur. J.* **2019**, *25*, 12659.
- [5] Y. Elani, *Angew. Chem., Int. Ed.* **2021**, *60*, 5602.
- [6] A. S. Zadorin, Y. Rondelez, G. Gines, V. Dilhas, G. Urtel, A. Zambrano, J.-C. Galas, A. Estevez-Torres, *Nat. Chem.* **2017**, *9*, 990.
- [7] K. Stephens, W. E. Bentley, *Trends Microbiol.* **2020**, *28*, 633.
- [8] H. Niederholtmeyer, C. Chaggan, N. K. Devaraj, *Nat. Commun.* **2018**, *9*, 5027.
- [9] J. W. Hindley, D. G. Zheleva, Y. Elani, K. Charalambous, L. M. C. Barter, P. J. Booth, C. L. Bevan, R. V. Law, O. Ces, *Proc. Natl. Acad. Sci. USA* **2019**, *116*, 16711.
- [10] Y. Qiao, M. Li, R. Booth, S. Mann, *Nat. Chem.* **2017**, *9*, 110.
- [11] S. Pérez-García, M. García-Navarrete, D. Ruiz-Sanchis, C. Prieto-Navarro, M. Avdovic, O. Pucciariello, K. Wabnik, *Nat. Commun.* **2021**, *12*, 4017.
- [12] C. E. Hilburger, M. L. Jacobs, K. R. Lewis, J. A. Peruzzi, N. P. Kamat, *ACS Synth. Biol.* **2019**, *8*, 1224.
- [13] T.-Y. D. Tang, D. Cecchi, G. Fracasso, D. Accardi, A. Coutable-Pennarun, S. S. Mansy, A. W. Perriman, J. L. R. Anderson, S. Mann, *ACS Synth. Biol.* **2018**, *7*, 339.
- [14] A. Dupin, F. C. Simmel, *Nat. Chem.* **2019**, *11*, 32.

- [15] O. Adir, M. R. Albalak, R. Abel, L. E. Weiss, G. Chen, A. Gruber, O. Staufer, Y. Kurman, I. Kamirer, J. Shklover, J. Shainsky-Roitman, I. Platzman, L. Gepstein, Y. Shechtman, B. A. Horwitz, A. Schroeder, *Nat. Commun.* **2022**, *13*, 2328.
- [16] V. Mukwaya, S. Mann, H. Dou, *Commun. Chem.* **2021**, *4*, 161.
- [17] S. Yang, P. A. Pieters, A. Joesaar, B. W. A. Bögels, R. Brouwers, I. Myrgorodska, S. Mann, T. F. A. de Greef, *ACS Nano* **2020**, *14*, 15992.
- [18] X. Ren, G. Zhong, Q. Zhang, L. Zhang, Y. Sun, Z. Zhang, *Cell Res.* **2020**, *30*, 763.
- [19] B. C. Buddingh', A. Llopis-Lorente, L. K. E. A. Abdelmohsen, J. C. M. van Hest, *Chem. Sci.* **2020**, *11*, 12829.
- [20] Ö. D. Toparlak, J. Zasso, S. Bridi, M. D. Serra, P. Macchi, L. Conti, M.-L. Baudet, S. S. Mansy, *Sci. Adv.* **2022**, *6*, abb4920.
- [21] I. Hwang, *Mol. Cells* **2013**, *36*, 105.
- [22] A. Joesaar, S. Yang, B. Bögels, A. van der Linden, P. Pieters, B. V. V. S. P. Kumar, N. Dalchau, A. Phillips, S. Mann, T. F. A. de Greef, *Nat. Nanotechnol.* **2019**, *14*, 369.
- [23] L. Tian, N. Martin, P. G. Bassindale, A. J. Patil, M. Li, A. Barnes, B. W. Drinkwater, S. Mann, *Nat. Commun.* **2016**, *7*, 13068.
- [24] G. Bolognesi, M. S. Friddin, A. Salehi-Reyhani, N. E. Barlow, N. J. Brooks, O. Ces, Y. Elani, *Nat. Commun.* **2018**, *9*, 1882.
- [25] T. Chakraborty, S. M. Bartelt, J. Steinkühler, R. Dimova, S. V. Wegner, *Chem. Commun.* **2019**, *55*, 9448.
- [26] T. Chakraborty, S. V. Wegner, *ACS Nano* **2021**, *15*, 9434.
- [27] O. I. Sentürk, E. Chervyachkova, Y. Ji, S. V. Wegner, *Small* **2019**, *15*, e1901801.
- [28] K. Han, D. Go, T. Tigges, K. Rahimi, A. J. C. Kuehne, A. Walther, *Angew. Chem., Int. Ed.* **2017**, *56*, 2176.
- [29] E. Chervyachkova, S. V. Wegner, *ACS Synth. Biol.* **2018**, *7*, 1817.
- [30] S. Zhang, T. Chen, N. Chen, D. Gao, B. Shi, S. Kong, R. C. West, Y. Yuan, M. Zhi, Q. Wei, J. Xiang, H. Mu, L. Yue, X. Lei, X. Wang, L. Zhong, H. Liang, S. Cao, J. C. I. Belmonte, H. Wang, J. Han, *Nat. Commun.* **2019**, *10*, 496.
- [31] X. Huang, M. Li, D. C. Green, D. S. Williams, A. J. Patil, S. Mann, *Nat. Commun.* **2013**, *4*, 2239.
- [32] M. Hörner, K. Gerhardt, P. Salavei, P. Hoess, D. Härrer, J. Kaiser, J. J. Tabor, W. Weber, *ACS Synth. Biol.* **2019**, *8*, 2442.
- [33] G. Guntas, R. A. Hallett, S. P. Zimmerman, T. Williams, H. Yumerefendi, J. E. Bear, B. Kuhlman, *Proc. Natl. Acad. Sci. USA* **2015**, *112*, 112.
- [34] N. Srinivas, J. Parkin, G. Seelig, E. Winfree, D. Soloveichik, *Science* **2017**, *358*, 2052.
- [35] L. Qian, E. Winfree, *Science* **2011**, *332*, 1196.
- [36] G. Seelig, D. Soloveichik, D. Y. Zhang, E. Winfree, *Science* **2006**, *314*, 1585.
- [37] L. Qian, E. Winfree, J. Bruck, *Nature* **2011**, *475*, 368.
- [38] J. Steinkühler, R. L. Knorr, Z. Zhao, T. Bhatia, S. M. Bartelt, S. Wegner, R. Dimova, R. Lipowsky, *Nat. Commun.* **2020**, *11*, 905.
- [39] D. Duguay, R. A. Foty, M. S. Steinberg, *Dev. Biol.* **2003**, *253*, 309.
- [40] A. Oyler-Yaniv, J. Oyler-Yaniv, B. M. Whitlock, Z. Liu, R. N. Germain, M. Huse, G. Altan-Bonnet, O. Krichevsky, *Immunity* **2017**, *46*, 609.
- [41] S. Sun, M. Li, F. Dong, S. Wang, L. Tian, S. Mann, *Small* **2016**, *12*, 1920.
- [42] L. Aufinger, F. C. Simmel, *Angew. Chem., Int. Ed.* **2018**, *57*, 17245.
- [43] A. M. Tayar, E. Karzbrun, V. Noireaux, R. H. Bar-Ziv, *Nat. Phys.* **2015**, *11*, 1037.
- [44] L. Tian, M. Li, J. Liu, A. J. Patil, B. W. Drinkwater, S. Mann, *ACS Cent. Sci.* **2018**, *4*, 1551.





## Supporting Information

for *Small*, DOI: 10.1002/smll.202206474

Orthogonal Light-Dependent Membrane Adhesion  
Induces Social Self-Sorting and Member-Specific DNA  
Communication in Synthetic Cell Communities

*Ali Heidari,\* Oya I. Sentürk,\* Shuo Yang,\* Alex Joesaar,\*  
Pierangelo Gobbo,\* Stephen Mann,\* Tom F. A. de  
Greef,\* and Seraphine V. Wegner\**

## Supporting Information

### **Orthogonal Light-dependent Membrane Adhesion Induces Social Self-sorting and Member-specific DNA Communication in Synthetic Cell Communities**

*Ali Heidari, Oya I. Sentürk, Shuo Yang, Alex Joesaar, Pierangelo Gobbo, Stephen Mann, Tom F.A. de Greef, Seraphine V. Wegner \**

#### **Materials and Methods**

1-(3-dimethylaminopropyl)-3-ethylcarbodiimide HCl (Sigma 98%), 2-Ethyl-1-hexanol (Sigma, 98%), 1,6-diaminohexane (Sigma, 98%), Rhodamine B isothiocyanate (RBITC, 70%, Sigma), PEG-bis(N-succinimidyl succinate) (MW=2000, Sigma), streptavidin from *Streptomyces avidinii* (Sigma), Atto425-Biotin (Sigma 95%), bovine serum albumin (heat shock fraction, pH=7.0, ≥98%, Sigma), Acryloyl chloride (≥97%, Sigma), *N*<sub>α</sub>*N*<sub>α</sub>-Bis(carboxymethyl)-L-lysine hydrate (≥97%, Sigma), Dowex resin 50WX8 (Sigma). All DNA oligonucleotides were purchased from Integrated DNA Technologies with HPLC purification, dissolved in 10 mM Tris (pH=8.0) and stored at -20 °C. All other reagents were purchased from Sigma Aldrich.

<sup>1</sup>H and <sup>13</sup>C spectra were recorded on a Varian 400 MHz spectrometer. <sup>1</sup>H NMR spectra are reported as δ in units of parts per million (ppm) relative to water or methanol (δ 4.65, s; δ 4.87, s respectively). The number of protons (*n*) for a given resonance is indicated as *n*H, and was based on spectral integration values. <sup>13</sup>C NMR spectra are reported as δ in units of parts per million (ppm) relative to CDCl<sub>3</sub> (δ 77.23, t).

UV-Vis spectroscopy experiments were performed using a PerkinElmer Lambda750 spectrophotometer using plastic cuvettes. Blanks were automatically subtracted from each spectrum.

Fourier transform infrared (FT-IR) spectra were recorded using a Perkin Elmer Spectrum One spectrophotometer equipped with an attenuated total reflectance sampling accessory. Polymer and protein-polymer conjugate samples were measured directly as solids, and the blank was automatically subtracted from each spectrum.

DLS and zeta-potential measurements were performed on a ZETASIZER Nano series instrument (Malvern Instruments, UK) using 1 mg/mL solutions of proteins or protein-polymer conjugates at pH 7.0 (10 mM PBS buffer).

Matrix-assisted laser desorption/ionization time of flight mass spectrometry (MALDI-TOF MS) was performed on a 4700 Proteomics analyzer (Applied Biosystems). The preparation of BSA, BSA/PNIPAM-co-NTA and PNIPAM-co-NTA samples required three solutions; (1) 3 equivalents of DHAP in EtOH (20.3 mg/mL) and 1 equivalent DAHC in water (18 mg/mL), (2) 2 vol% TFA

in water, and (3) 2-3 mg/mL of protein, polymer or protein-polymer conjugate in water. The three solutions were mixed in 1:1:1 volume ratio and spotted on the MALDI plate.

For all the experiments, red light (Albrillo LL-GL003, 225 LEDs, 660 nm, 14 W, 544  $\mu\text{W}/\text{cm}^2$ ) LED light panel, and blue light (Albrillo LL-GL003, 225 LEDs, 480 nm, 14 W, 544  $\mu\text{W}/\text{cm}^2$ ) were used.

### **Expression and purification of proteins**

The plasmids pQE-80L iLID (C530M) and pQE-80L MBP-SspB Nano were gifts from Brian Kuhlman (Addgene # 60408 and 60409, respectively)<sup>[1]</sup>. The N-terminal His6-tagged iLID and Nano proteins were expressed and purified as previously reported.<sup>[2]</sup> PhyB protein was encoded in the plasmid pMH1105 (a gift from Dr. Maximilian Hörner and Prof. Wilfried Weber) was expressed and purified through its His-tag following the reported protocol.<sup>[3]</sup> The PIF6-GFP-His6-tag in pET21b vector was expressed and purified as previously described.<sup>[4]</sup> His-GFP (N-terminally His6-tagged, Addgene # 29663) was recombinantly expressed in *E. coli* and purified over a  $\text{Ni}^{2+}$ -NTA column using standard protocols. The purity of the proteins was verified using SDS-PAGE and the protein concentrations were determined by UV-vis spectroscopy.

### **Synthesis of 2,20-(5-acrylamido-1-carboxypentylazanediy)diacetic acid (NTA-acrylate) (1)**

The synthesis was carried out using a modified version of the procedure of M. Ehrbar and co-workers.<sup>[5]</sup>  $N_{\alpha},N_{\alpha}$ -Bis(carboxymethyl)-L-lysine hydrate (0.7868 mg, 3 mmol) was dissolved in 27 mL of 0.44 M NaOH and the solution was cooled to 0 °C. Acryloyl chloride (0.322 mL, 4.0 mmol) was dissolved in 15 mL of dry toluene and added dropwise to the cold solution of  $N_{\alpha},N_{\alpha}$ -Bis(carboxymethyl)-L-lysine. The biphasic solution was vigorously stirred overnight at room temperature. The morning after the reaction mixture was transferred into a separatory funnel, and the toluene layer discarded. The aqueous layer was then washed two more times with toluene to remove the excess acryloyl chloride. The aqueous layer was then distilled down to a few mL, transferred into a 50 mL plastic test-tube, and diluted to 30 mL with MilliQ water. To this solution 10 mL of Dowex 50WX8 resin were added and the solution was gently shaken for 30 min. The resin was then removed through gooch filtration on a bed of sand and washed with MilliQ water until the pH of washes was neutral. The resulting clear aqueous solution containing the product was concentrated down to a few mL and lyophilised.

$^1\text{H}$  NMR (400 MHz,  $\text{D}_2\text{O}$ ):  $\delta$  6.11 (dd,  $J_a = 16$  Hz,  $J_b = 8$  Hz, 1H), 6.01 (d,  $J = 16$  Hz, 1H), 5.59 (d,  $J = 16$  Hz, 1H), 4.00 (s, 4H), 3.96 (dd,  $J_a = 12$  Hz,  $J_b = 4$  Hz 1H), 3.14 (t,  $J_a = 8$  Hz, 2H), 1.91-1.74 (m, 2H), 1.52-1.32 (m, 4H).  $^{13}\text{C}$  NMR (128 MHz,  $\text{CDCl}_3$ ):  $\delta$  170.4, 169.0, 168.3, 130.0, 127.0, 66.9, 54.1, 38.6, 27.7, 26.4, 22.7. HRMS ( $m/z$ ): calcd. for  $\text{C}_{13}\text{H}_{21}\text{N}_2\text{O}_7$   $[\text{M}+\text{H}]^+$ , 317.1343; found, 317.1329.

### **Synthesis of mercaptothiazoline-activated PNIPAM-co-NTA (2)**

*N*-isopropylacrylamide and AIBN were freshly recrystallized from hexane and methanol, respectively. Mercaptothiazoline-activated RAFT agent was synthesised according to our

previously established procedure.<sup>[6]</sup> *N*-isopropylacrylamide (0.450 g; 3.98 mmol), NTA-acrylate (50 mg, 0.16 mmol; 4 mol%, 10 wt%), and AIBN (30 mg, 0.18 mmol) were dissolved in 3 mL of methanol, and added to a small round bottom flask equipped with a stirrer bar. To this solution mercaptothiazoline-activated RAFT agent (12.8 mg, 34.5  $\mu$ mol) dissolved in 1 mL of acetonitrile was added. The solution was purged with argon for 30 min and the flask sealed. Polymerization was carried out at 65 °C for 8 h with stirring at 700 rpm. The polymer was isolated by precipitation from 1:1 hexane/Et<sub>2</sub>O (250 mL) as a crystalline light-yellow powder in 96 wt% yield.  $M_n$  5760 g mol<sup>-1</sup>,  $M_w$  5800 g mol<sup>-1</sup>, PDI 1.01, 5 mol% in NTA-acrylate. See Supplementary figure 2 for <sup>1</sup>H and <sup>13</sup>C NMR spectra. From the integration reported in Supplementary figure 2 and molecular weight of the polymer it is possible to calculate that in average the polymeric chains are composed by 44 NIPAM units and 3 NTA units.

The LCST was estimated through UV-Vis turbidity measurements, and by acquiring the transmittance between 550 and 600 nm of a 1 mg mL<sup>-1</sup> polymer solution in MilliQ water. Data points were acquired at different temperatures from 25 to 45 °C, and 5 min of equilibration time was waited between the spectrum acquisitions. The experiment was repeated in triplicate. The cloud point temperature ( $T_{cp}$ ), taken as the 50% of the initial transmittance value, was determined to 34 °C, see figure S9.

### **Preparation of BSA/PNIPAM-co-NTA conjugates**

*Labelling of BSA with fluorescent dyes:* In general, 20.9 mg of BSA were dissolved in 7.74 mL of Na<sub>2</sub>CO<sub>3</sub> buffer (pH 8.5, 100 mM), and 193.5  $\mu$ L of a DMSO solution of a Rhod B isothiocyanide dye (1.0 mg/mL) added. The conjugation reaction was performed for 5 h at room temperature. The Rhod B-conjugated BSA was purified by dialysis using 12-14 kDa MWCO membranes, lyophilized and stored as a solid at -20 °C.

*Cationization of BSA:* In a vial, 18 mg of unlabelled or RhodB-labelled BSA were dissolved in 1.8 mL of water. In a separate vial, 180 mg of hexamethylenediamine were dissolved in 1.8 mL of water and the pH was adjusted to 6.0. The hexamethylenediamine solution was slowly added to the BSA solution under vigorous stirring, and the pH readjusted to 6.0. The cationization reaction was initiated by adding 9.0 mg of EDAC dissolved in 500  $\mu$ L of water. After 2 h, another 9 mg of EDAC dissolved in 500  $\mu$ L of water were added. The reaction was left under stirring at room temperature for 18 h. BSA-NH<sub>2</sub> was purified by dialysis, centrifuged (5 min, 5000 rpm) to remove any precipitate, and then lyophilised and stored as a solid at -20 °C. On average, this procedure resulted in a 30 % level of cationization as determined by MALDI-TOF spectrometry.

*BSA/PNIPAM-co-NTA:* In a vial, 20 mg of unlabelled or RBITC-labelled cationized BSA were dissolved in 10 mL of Na<sub>2</sub>CO<sub>3</sub> buffer (pH 8.5, 100 mM). In a separate vial, 20 mg of mercaptothiazoline-activated PNIPAM-co-NTA were dissolved in 10 mL of water. The mercaptothiazoline-activated PNIPAM-co-NTA solution was added dropwise to a stirred solution of cationized BSA, and the conjugation reaction carried out for 18 h at room temperature. BSA/PNIPAM-co-NTA conjugate was then isolated by centrifugation using centrifugal filters

with 50 kDa MWCO. The residues were washed 4 times to remove any unreacted polymer, and the product lyophilised and stored as a solid at -20 °C.

### **Preparation of the streptavidin-containing Ni<sup>2+</sup>-NTA proteinosomes**

7.5 µL of BSA/PNIPAM-co-NTA conjugates (final concentration: 16 mg/ml) and 4.2 µL streptavidin (final concentration: 10 µM) dissolved in buffer (50 mM sodium carbonate pH 8.5) were mixed in an Eppendorf tube and 1.5 mg of PEG-bis (*N*-succinimidyl succinate) (M<sub>w</sub> = 2000, Sigma) dissolved in 3.3 µL buffer was added to the mixture. Afterwards, a Pickering emulsion was produced by adding 600 µL of 2-ethyl-1-hexanol and vortexing for 25 s. The sample was kept for at least 3 h at room temperature in the dark for the crosslinking reaction to take place. The upper oil layer was removed and then, the emulsion was dispersed into 400 µL of 70% ethanol and dialyzed sequentially in 70% ethanol (2 h), 50% ethanol (4 h) and water (overnight). The proteinosomes suspension was stored at 4 °C. For the loading of the NTA groups with Ni<sup>2+</sup> ions, were the resulting proteinosomes in water dialyzed against 10 mM NiCl<sub>2</sub> for 3 h, at 4 °C. The excess NiCl<sub>2</sub> was dialyzed away against water overnight at 4 °C.

10 µL of the FITC-labeled streptavidin solutions with 3.5 µM, 7.5 µM, and 15 µM concentrations were fixed between the coverslips. The intensity values were measured using the same settings on the confocal microscope as for the proteinosomes. The streptavidin concentration in the proteinosomes was fitted to the calibration curve.

### **Localization of DNA complexes in streptavidin-containing proteinosomes**

Following the previously published protocols,<sup>[7,8]</sup> the DNA gate complexes were loaded into proteinosomes in 10 mM Tris Buffer pH 8.0 with 12 mM Mg<sup>2+</sup> and 0.1% v/v Tween 20. Typically, a dispersion of streptavidin-containing proteinosomes (10 µL), and 2 µL of biotinylated F strands (final concentration 1.2 µM) were gently mixed and incubated at room temperature for 1 h. Then 2 µL of the corresponding quencher strands Q (final concentration: 1.6 µM) was added to the mixture and incubated at 4°C overnight. Subsequently, for labeling the R2 proteinosomes, 5 µL of 500 nM Atto425-biotin solution was added to 10 µL of receiver proteinosomes and incubated for 10-15 min at room temperature. To remove the excess strands, 10 µL of the supernatant was removed carefully from the top and 10 µL buffer was added. Proteinosomes were allowed to sediment for 7 h at 4°C and 10 µL supernatant from the top was removed and 400 µL buffer were added. The proteinosomes suspension was allowed to sediment for 7-8 h and the top 380 µL of buffer were removed. The resulting DNA gate loaded proteinosomes were stored at 4°C.

### **Protein immobilization on the proteinosomes**

In the dark, 1 µL BSA (stock concentration 2 mg/mL) was added to 10 µL of Ni<sup>2+</sup>-NTA/PNIPAM proteinosomes (loaded with DNA gate complexes beforehand where necessary) and incubated for 5 min at room temperature. Then, 2 µL of His-tagged protein (total final concentration 500 nM) were added to the mixture and the sample was incubated room temperature for 10-20 min. iLID

and PhyB proteins were added in equal portions at the same time for the functionalization of the S proteinosome and PIF6 and Nano were added to R1 and R2 proteinosomes, respectively.

### **Surface density of proteins on the proteinosomes**

Following the previously reported protocol,<sup>[9]</sup> the surface density of proteins on proteinosomes was quantified by functionalizing the proteinosomes with different concentration of His6-tagged GFP (His6-GFP) and comparing the fluorescent signal of the membrane bound protein on the proteinosomes with GUV membrane prepared with 1 mol% DGS-NTA. The average fluorescence intensity along the vesicle contour was measured using the (Radial Profile Extended plugin, Philippe Carl). The fluorescent background level was estimated from micrographs where DGS-NTA or PNIPAM-co-NTA were absent for GUVs and proteinosomes, respectively. Finally, by taking the area per lipid a conversion factor was obtained, which was then used to convert membrane fluorescent intensities to GFP surface coverage on proteinosomes.

The experimental data are well fitted by the linear relationship  $\Gamma = (67 \pm 2) \times \mu\text{m}^{-2} \text{ nM}^{-1}$  for GUVs and  $\Gamma = (109 \pm 8) \times \mu\text{m}^{-2} \text{ nM}^{-1}$  for proteinosomes over the concentration range of  $0 < X \leq 23 \text{ nM}$ . Consequently, the GFP concentration  $X = 500 \text{ nM}$  leads to the coverage of  $\Gamma = 4949 \mu\text{m}^{-2}$ .

### **Light-triggered aggregation of the 2- and 3- membered proteinosome mixtures**

10  $\mu\text{L}$  S proteinosomes were mixed with 10  $\mu\text{l}$  of R1 or R2 proteinosomes in 2-membered communities or with 5  $\mu\text{L}$  of R1 and 5  $\mu\text{l}$  of R2 proteinosomes for 3-membered communities with 8  $\mu\text{l}$  3.5x DNA buffer (final buffer concentrations: 10 mM Tris pH 8, 12 mM  $\text{MgCl}_2$ , 0.05% v/v Tween 20) in a  $\mu\text{-Slide}$  18 Well-Flat uncoated glass bottom dish (Ibidi GmbH, Martinsried, Germany). Afterward, the different samples were incubated for 90 min in the dark, under blue or red light (120 s ON, 360 s OFF) while shaking on a 2D shaker at 30 rpm. The proteinosomes were allowed to settle for 20-30 min before imaging.

For two membered communities, an area of  $0.5 \times 0.5 \text{ mm}^2$  was imaged for each sample in the RhodB channel to visualize all proteinosomes. For analyzing the aggregation ratio, the images were converted into binary images and holes were filled using the “Fill holes” tool. Then, the area occupied by different proteinosomes, and their clusters (objects) was quantified using the “Analyze particle tool”. Objects larger than  $2000 \mu\text{m}^2$  were considered as aggregates. Then proteinosomes within a cluster were separated by a 1 pixel line using the “Watershed” function. The number of proteinosomes in each sample was determined using the “Analyze Particle” function. Then the aggregation ratio was calculated from dividing the number proteinosomes in the cluster by the total number of proteinosomes in the sample.

For three membered communities, first the DSD reaction was carried out and at the end an area of  $0.5 \times 0.5 \text{ mm}^2$  was imaged in the Rhod B (all proteinosomes), Atto425 (R2 proteinosomes), Alexa488 (S proteinosomes) and Cy5 (activated R proteinosomes) channels. The data was used to analyze both the aggregation ratio (see below) and the communication different populations.

### **DNA-Stand-Displacement (DSD) cascade**

The proteinosome samples were allowed to aggregate under different illumination conditions as described above and were settled for 20-30 min. To start the DSD reaction, 2  $\mu$ L fuel strand (final concentration: 670 nM) and 2  $\mu$ L of the input strand (final concentration: 100 nM)<sup>[8, 9]</sup> were added. The samples were imaged every 1 min for 70 min the Alexa488 (S activation) and Cy5 (R activation) channels using confocal microscopy. In 2-membered communities, the mean fluorescence in the Alex488 and Cy5 channels over time was analyzed for  $n > 45$  randomly picked S and R proteinosomes, respectively and corrected for the background.

### **Image analysis in three membered communities**

To analyze the aggregation behaviour of different pairs in the 3-membered community, first brightness and contrast in the different channels was adjusted (S+R1+R2=Rhod B, S=Alexa488, R2=Atto425, and activated R=Cy5) and different channels were used to compute the area occupied by different pairs (S+R1=Rhod B – Atto425, S+R2=Alexa488+Atto425, R1+R2=Rhod B – Alexa488). Subsequently, the images were converted into binary images and the clustered proteinosomes were detected using the “Analyze Particles” function, where only objects with an area  $> 2000 \mu\text{m}^2$  were considered as aggregates. Then proteinosomes within a cluster were separated by a 1 pixel line using the “Watershed” function. The number of proteinosomes was determined using the “Analyze Particle” function. Finally, the aggregation ratio was calculated from dividing the number proteinosomes in the cluster by the total number of proteinosomes in the sample (Rhod B channel).

To analyze the communication within the three membered community, the images acquired in different channels were converted to binary images and interior of the proteinosomes was filled using the “Fill hole” function in ImageJ. A mask was created from the binary images using “Convert to mask” function and then proteinosomes within a cluster were separated by a 1 pixel line using the “Watershed” function. The number of proteinosomes in each population was determined using the “Analyze Particle” function. The activated R2 proteinosomes were defined as the overlap of the Atto425 and Cy5 channels, the activated R1 proteinosomes as the difference of the Cy5 from the Atto425 channels and the non-responders as the difference of the Rhod B channel from the Alexa488 and Cy5 channels. Finally, the population ratio was calculated by dividing the number of each population by the total number of proteinosomes in the sample.

### **Signal propagation in sender proteinosome**

The F1 and F3 DNA strands were loaded into the sender proteinosome, and they were subsequently functionalized with iLID and PhyB proteins following the protocol described above. The DSD reaction was initiated, and the samples were imaged every 1 min for 60 min using the Cy5 channel (F3 signal strand) and Alexa488 (F1 strand) on confocal microscopy. The mean fluorescence intensity in the Cy5 channel across a horizontal line over time was analyzed and corrected for the background.

## Measuring the diffusion of DNA signal through the proteinosome membrane

First, the control channels of microfluidic device were filled with MilliQ water and the pressure was set at 2 bar and the microfluidic tapping device was mounted on the stage of a confocal microscope (CLSM, Leica SP8). The pressure to the inlet channels was adjusted using adjustable pressure regulators (Flow-EZ, Fluigent). The buffer solution was connected to inlet 1. By closing all other inlet and outlet valves, and pressurizing the buffer channel at 1 bar, air bubbles were pushed out of the flow channels followed by thoroughly washing all the flow channels using the buffer solution. DNA-containing proteinosomes were loaded from the inlet 2 into the tapping array at a pressure of 10 mbar, Then the inlet 2 was closed and the proteinosomes were gently washed using ca. 5-15 mbar with buffer solution for 5-10 min to remove any unbound DNA. All experiments were performed at room temperature and the initial steady-state signals were recorded as the baseline values.

The DNA oligonucleotides were diluted in buffer solution with 2 mg/ml BSA to minimize DNA adsorption to tubing and loaded to inlet 3. Using 10 mbar pressure for 20 s, the DSD reactions were started and the pressure was then reduced to 3 mbar to maintain a slow flow (ca. 0.1  $\mu\text{L}/\text{min}$ ) of DNA strand solution into the trapping chamber and thereby a constant input concentration in the extra extracellular medium. Estimation of proteinosome permeability and the rate constant was calculated using the mathematical model described before.<sup>[8]</sup>

## Data acquisition, and statistical analysis

All confocal microscopy images were acquired on a Leica DMi8 S laser scanning confocal microscope, equipped with 405, 488, 552 and 638 nm lasers and 20x/0.75 NA, 20x/0.75 IMM or 40x/1.10 W CS2 (field of view: 0.775x0.775 mm<sup>2</sup>, slice thickness: 2 $\mu$ ) objectives. All microscopy images were analyzed using the ImageJ 1.52b and LASX software. All values were reported as the mean  $\pm$  SEM, from three independent replicates. Significant differences between groups were analyzed using an unpaired t-test, \*p < 0.05, \*\*p < 0.01, and \*\*\*p < 0.001.

	DNA sequence (5' $\longrightarrow$ 3')	Number of bases	5' modification	3' modification
<b>Input (A)</b>	TAT TAC AGC GAA CGA ACG ACA CTA ATG CAC TAC TAC	36		
<b>F1</b>	GTA GTA GTG CAT TAG TGT CGT TCG TTC GCT GTA ATA	36	Alexa488	Biotin-TEG
<b>F2</b>	GCA TTA GTC TAT CAT GGT CGT TCG TTC GAC AGT TCC	36	Biotin-TEG	Cy5
<b>Q1</b>	CGA ACG AAC GAC CAT GAT AGA CTA ATG CAC TAC TAC	36		Iowa Black
<b>Q2</b>	GGA ACT GTC GAA CGA ACG TGA AAC CGA CCA TGA TAG	36	Iowa Black	phosphate
<b>F3</b>	CGA ACG AAC GAC CAT GAT AGA CTA ATG CAC TAC TAC	36		Cy5
<b>Fuel</b>	GGA ACT GTC GAA CGA ACG ACC ATG ATA G	28		phosphate

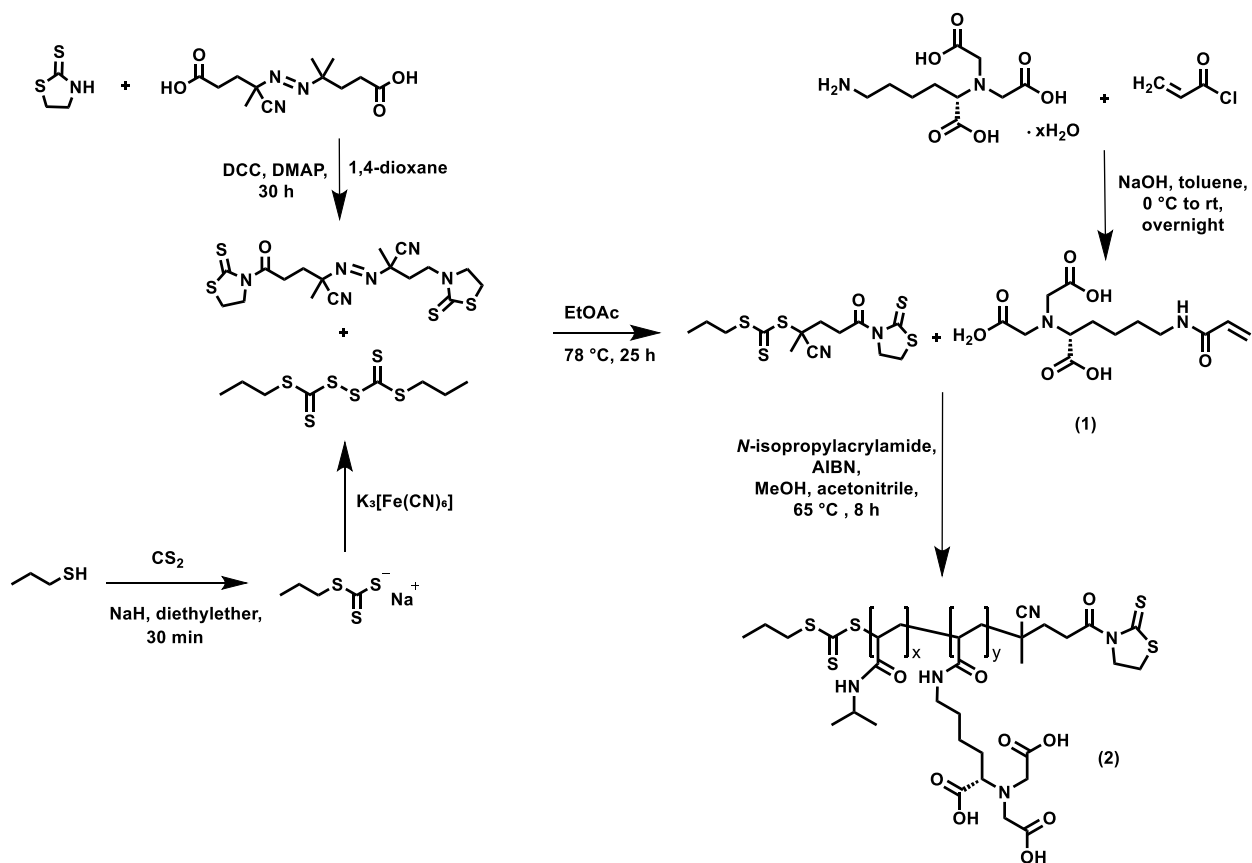
**Table S1.** DNA sequences used for DSD reactions in proteinosomes.

## Supplemental References

- [1] G. Gurkan, H. R. A., Z. S. P., W. Tishan, Y. Hayretin, B. J. E., K. Brian, *Proc. Natl. Acad. Sci.* **2015**, *112*, 112.
- [2] E. Chervyachkova, S. V Wegner, *ACS Synth. Biol.* **2018**, *7*, 1817.



- [3] M. Hörner, O. S. Yousefi, W. Schamel, W. Weber, *Bio-Protocol* **2020**, *10*, 1.
- [4] O. I. Sentürk, O. Schauer, F. Chen, V. Sourjik, S. V. Wegner, *Adv. Healthc. Mater.* **2020**, *9*, 1900956.
- [5] M. Ehrbar, R. Schoenmakers, E. H. Christen, M. Fussenegger, W. Weber, *Nat. Mater.* **2008**, *7*, 800.
- [6] X. Huang, M. Li, D. C. Green, D. S. Williams, A. J. Patil, S. Mann, *Nat. Commun.* **2013**, *4*, 1.
- [7] S. Yang, P. A. Pieters, A. Joesaar, B. W. A. Bögels, R. Brouwers, I. Myrgorodska, S. Mann, T. F. A. de Greef, *ACS Nano* **2020**, *14*, 15992.
- [8] A. Joesaar, S. Yang, B. Bögels, A. van der Linden, P. Pieters, B. V. V. S. P. Kumar, N. Dalchau, A. Phillips, S. Mann, T. F. A. de Greef, *Nat. Nanotechnol.* **2019**, *14*, 369.
- [9] J. Steinkühler, R. L. Knorr, Z. Zhao, T. Bhatia, S. M. Bartelt, S. Wegner, R. Dimova, R. Lipowsky, *Nat. Commun.* **2020**, *11*, 905.
- [10] D. Y. Zhang, E. Winfree, *Nucleic Acids Res.* **2010**, *38*, 4182.



**Scheme S1.** Synthesis of end-capped mercaptothiazoline-activated PNIPAM-co-NTA by RAFT polymerization. The end-capped mercaptothiazoline-activated PNIPAM was synthesized by reversible addition-fragmentation chain-transfer (RAFT) polymerization using a designed trithiol RAFT agent.<sup>[6]</sup>

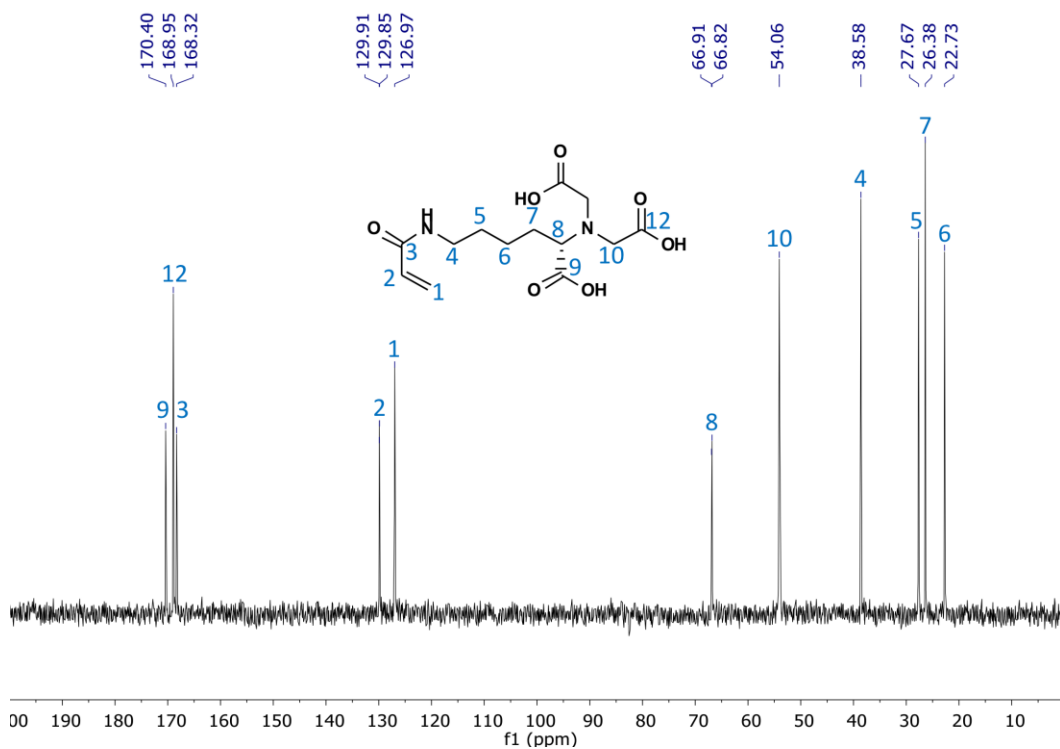
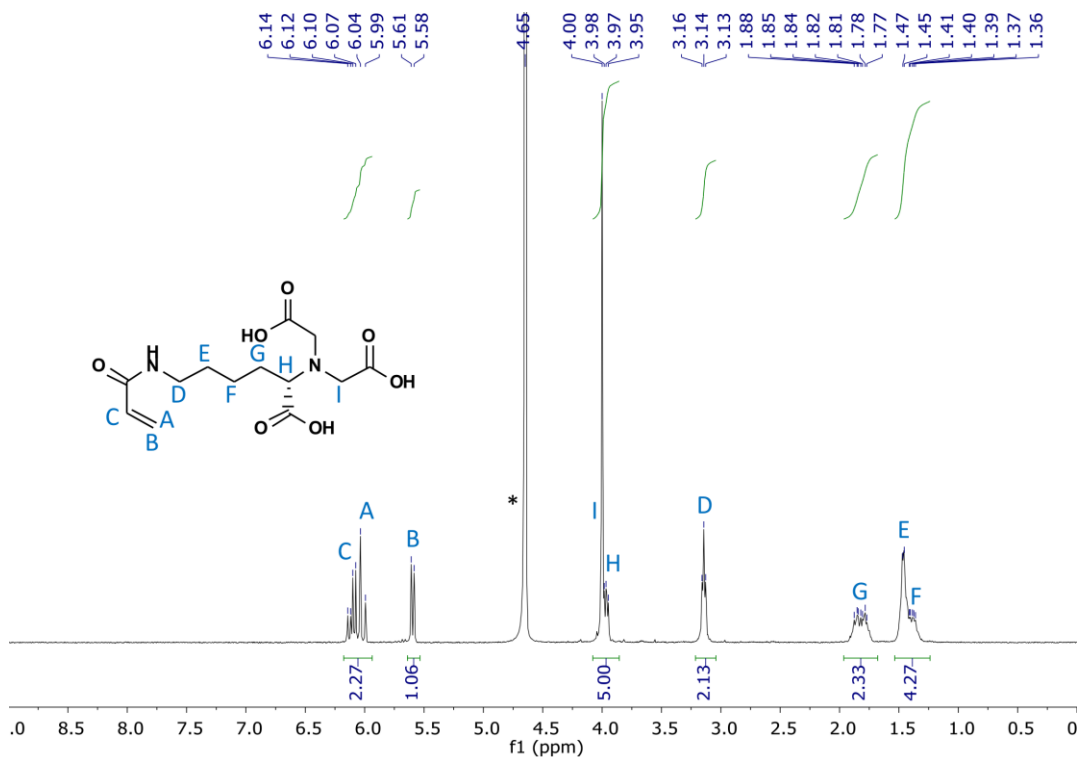
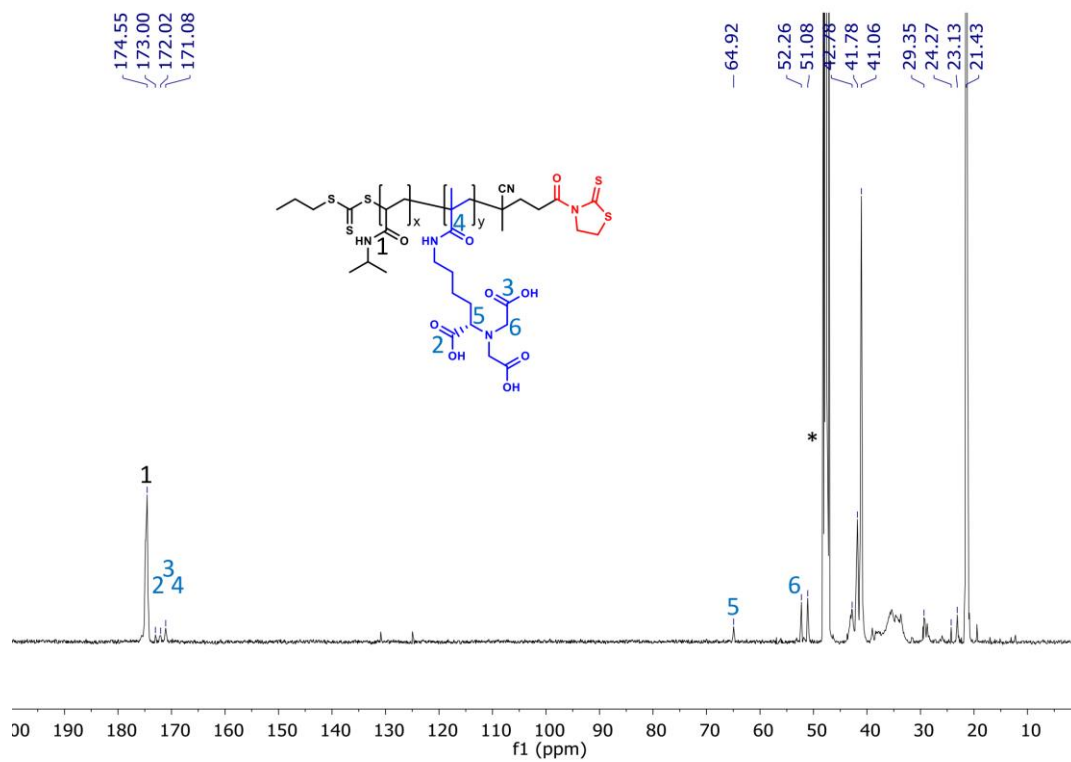
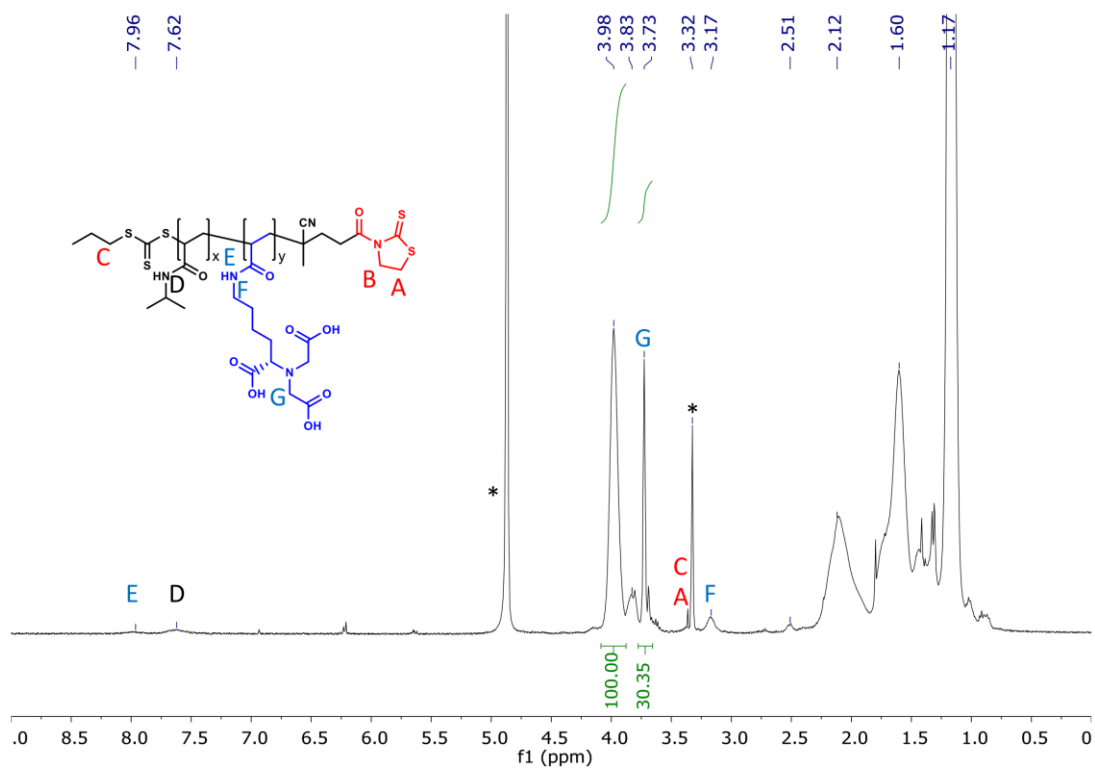
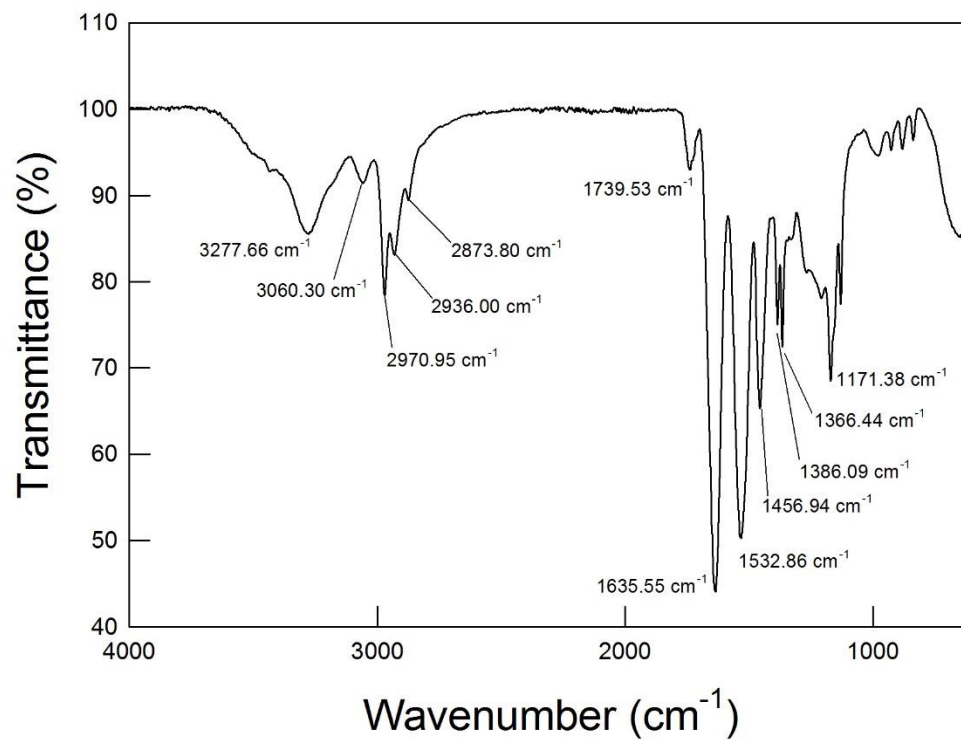


Figure S1. <sup>1</sup>H NMR (top) and <sup>13</sup>C NMR (bottom) spectra of 2,20-(5-acrylamido-1-carboxypentylazanediyl)diacetic acid (NTA-acrylate) (1). Spectra acquired in D<sub>2</sub>O as the solvent and calibrated against residual protonated solvent (\*).



**Figure S2.**  $^1\text{H}$  NMR (top) and  $^{13}\text{C}$  NMR (bottom) spectra of PNIPAM-co-NTA (2). Spectra acquired in  $\text{CD}_3\text{OD}$  as the solvent and calibrated against residual protonated solvent (\*).



**Figure S3. FT-IR spectrum of PNIPAM-co-NTA showing a carbonyl peak at 1739.53 cm<sup>-1</sup> that indicates successful incorporation of NTA in the polymeric chain.**

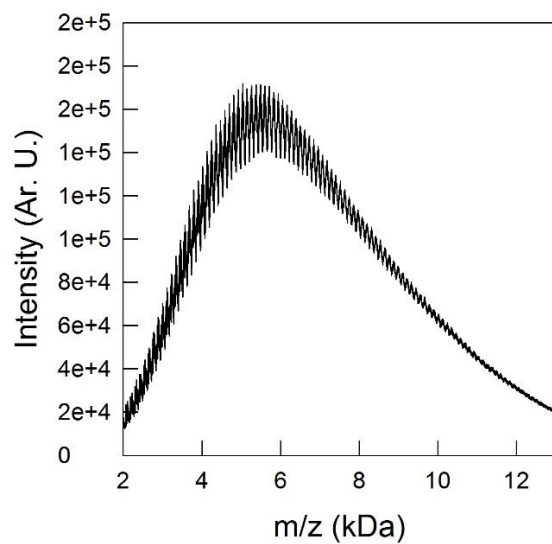


**Figure S4. MALDI spectrum of PNIPAM-co-NTA showing  $M_n$  5760 g mol<sup>-1</sup>,  $M_w$  5800 g mol<sup>-1</sup>, PDI 1.01.**

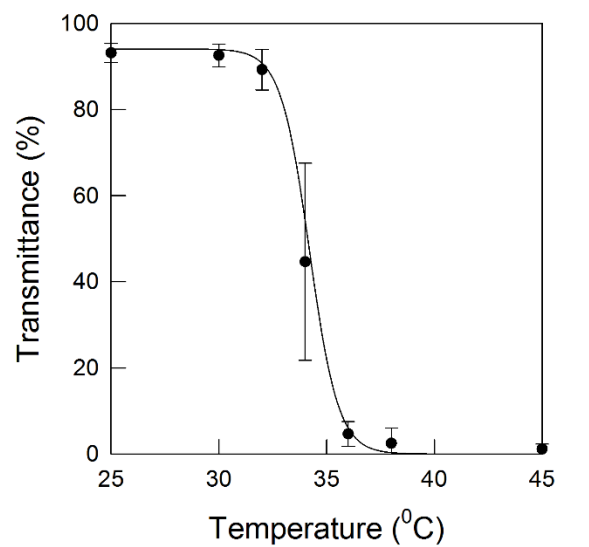


**Figure S5. Estimation of LCST for PNIPAM-co-NTA.** The cloud point temperature ( $T_{cp}$ ) was determined by measuring the transmittance between 500 and 600 nm for a polymer solution in water at a concentration of  $1 \text{ mg mL}^{-1}$ . The  $T_{cp}$ , taken as the 50% of the initial transmittance value, was determined to be  $34 \text{ }^\circ\text{C}$ .

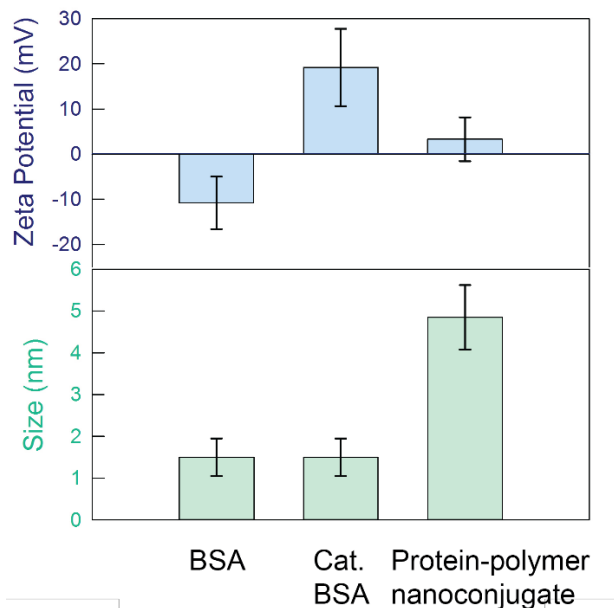


**Figure S6. Zeta potential (top) and hydrodynamic diameter (bottom) measurements of native BSA, cationized BSA and BSA/PNIPAM-co-NTA conjugate.** Measurements carried out using  $1 \text{ mg mL}^{-1}$  solutions of protein or protein-polymer conjugate in 10 mM PBS buffer pH 7.0. Measurements repeated in triplicate and error bars are standard deviation of the mean. Passing from cationized BSA to protein-polymer conjugate it is evident a marked decrease in surface charge and increase in hydrodynamic diameter, confirming a successful conjugation of PNIPAM-co-NTA to cationized BSA.



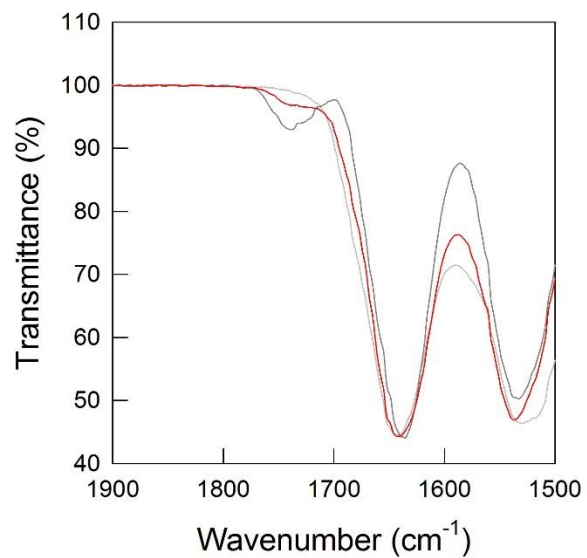


**Figure S7. FT-IR carbonyl region of BSA (light grey), PNIPAM-co-NTA (dark grey), and BSA/PNIPAM-co-NTA (red), showing successful conjugation of PNIPAM-co-NTA to cationized BSA.**

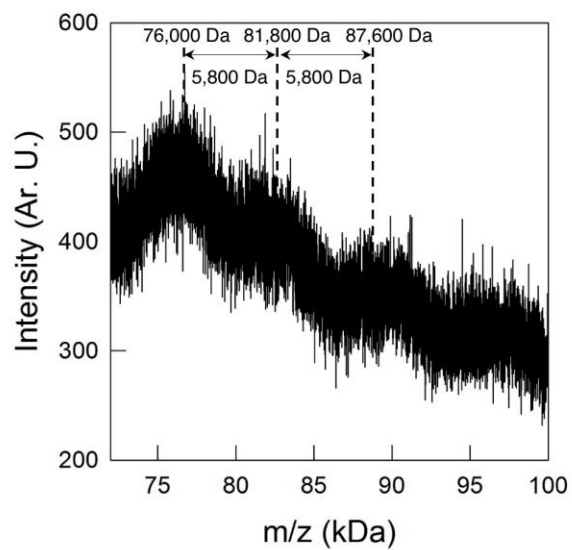


**Figure S8. MALDI spectrum of BSA/PNIPAM-co-NTA conjugate showing successful conjugation of at least 3 polymer chains to a single cationized BSA centre.**

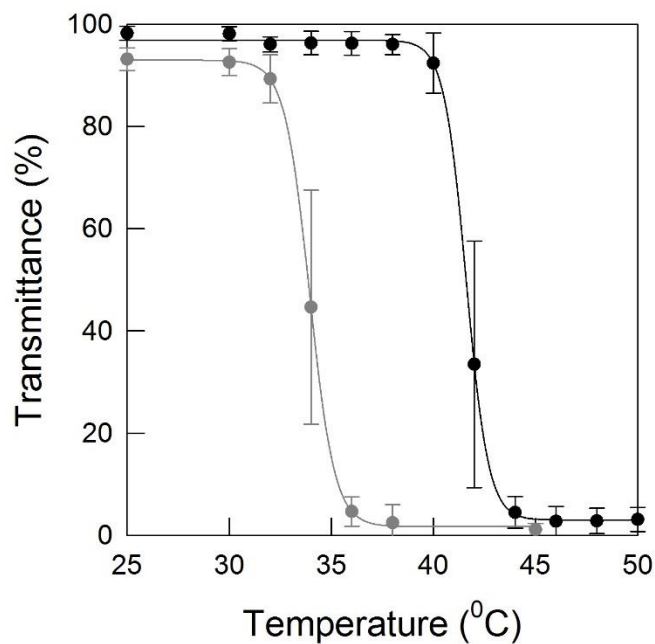


**Figure S9. Estimation of LCST for PNIPAM-co-NTA (grey) and of BSA/PNIPAM-co-NTA conjugate (black).** The cloud point temperature ( $T_{cp}$ ) was determined by measuring the transmittance between 500 and 600 nm for a polymer or conjugate solution in water at a concentration of  $1 \text{ mg mL}^{-1}$ . The  $T_{cp}$ , taken as the 50% of the initial transmittance value, was determined to be  $34.0 \text{ }^{\circ}\text{C}$  and  $41.5 \text{ }^{\circ}\text{C}$  for PNIPAM-co-NTA and of BSA/PNIPAM-co-NTA conjugate, respectively.

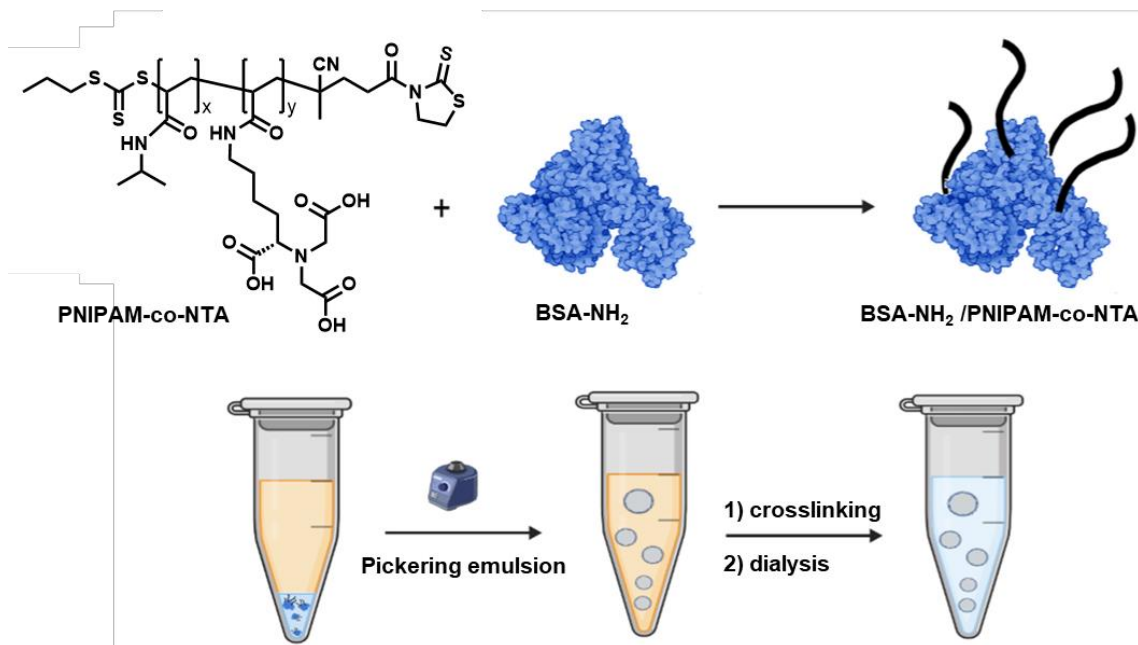


**Figure S10. General procedure for preparation of proteinosomes.** Cationized bovine serum albumin (BSA-NH<sub>2</sub>) is synthesized via the previously reported procedure.<sup>[6]</sup> Coupling of mercaptothiazoline-activated PNIPAM-co-NTA polymer chains with primary amine groups with cationized BSA-NH<sub>2</sub> gives protein-polymer conjugates (BSA-NH<sub>2</sub>/PNIPAM-co-NTA). Carbodiimide-activated cationization of the aspartic and glutamic acid residues using the 1-6, hexandiamine enhanced the number of accessible amine groups available on the surface as well as the post-synthetic crosslinking. Micro-droplets were stabilized by a monolayer of closely packed protein-polymer conjugates and then crosslinked by using O,O'-Bis[2-(N-Succinimidylsuccinylamino)ethyl]polyethylene glycol (Mw 2,000; Sigma) at the water/oil droplet interface, and transferred into aqueous solution by removing the oil using a series of dialysis against water/ethanol mixtures.

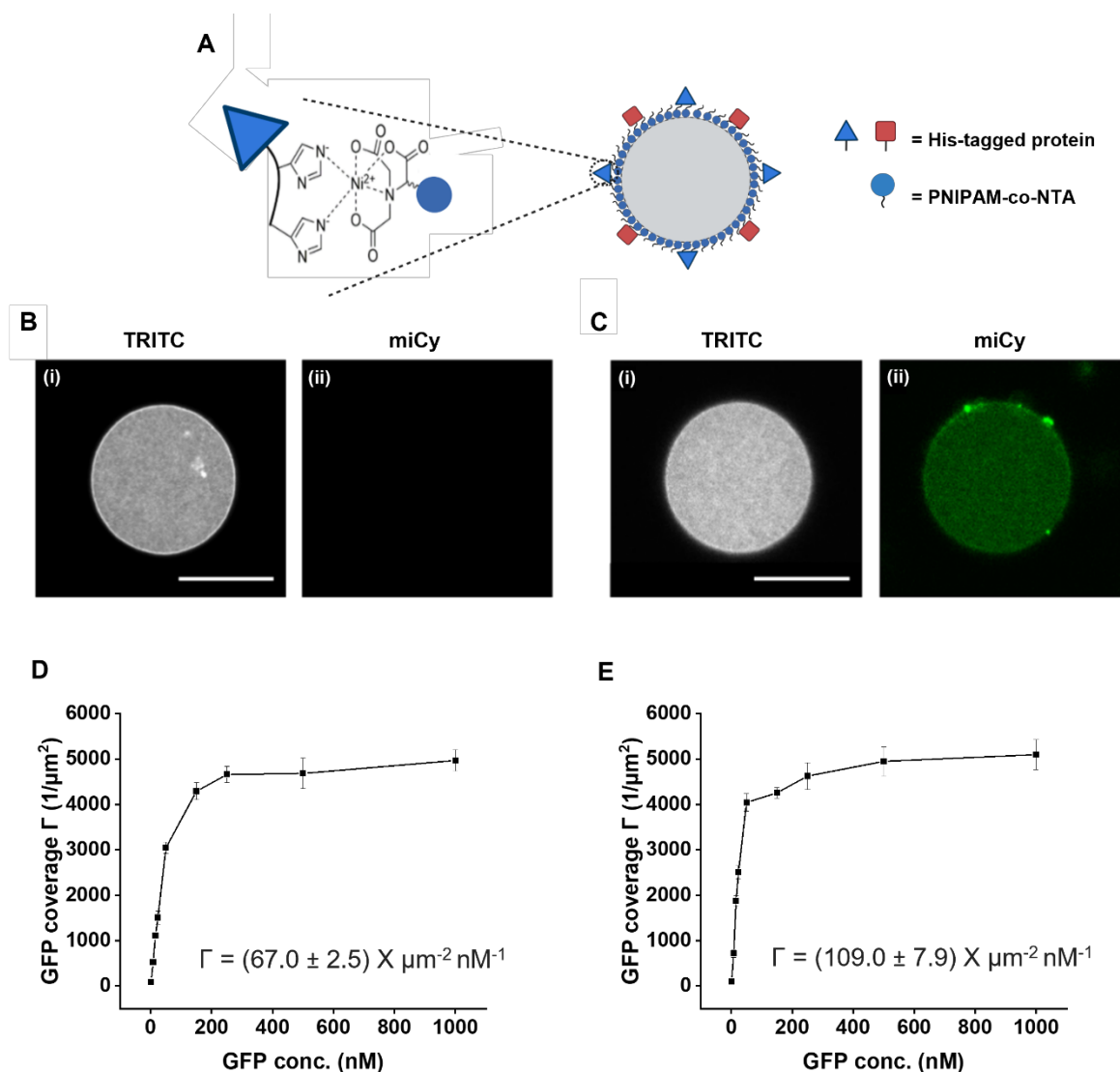


**Figure S11. Surface functionalization of proteinosomes with His-tagged proteins.** A)  $\text{Ni}^{2+}$ -NTA groups on the surface of the proteinosomes bind to His-tagged proteins through the formation of the corresponding coordination complex after 20 min incubation. Confocal microscopy images in the i) Rhod B and ii) miCy channels for B) not loaded and C)  $\text{Ni}^{2+}$  loaded NTA-PNIPAM proteinosomes. miCy fluorescence only being visible in the  $\text{Ni}^{2+}$  loaded proteinosomes demonstrates the specific immobilization through the His-tag. The scale bars are 50  $\mu\text{m}$ . Relation between solution His6-GFP concentration  $X$  and membrane bound His6-GFP density  $\Gamma$  for D) GUVs with 1 mol% DGS-NTA- $\text{Ni}^{2+}$  and E) 1 mol% PNIPAM-co-NTA proteinosomes (see methods). The linear fit for GUVs is  $\Gamma = (67 \pm 2) \times \mu\text{m}^{-2} \text{nM}^{-1}$  ( $R^2 = 9.99$ ) over the range of  $0 < X \leq 23$  nM and for proteinosomes is  $\Gamma = (109 \pm 8) \times \mu\text{m}^{-2} \text{nM}^{-1}$  ( $R^2 = 9.98$ ) over the range of  $0 < X \leq 23$  nM. Error bars show the std. dev. of the mean ( $n=3$ ).

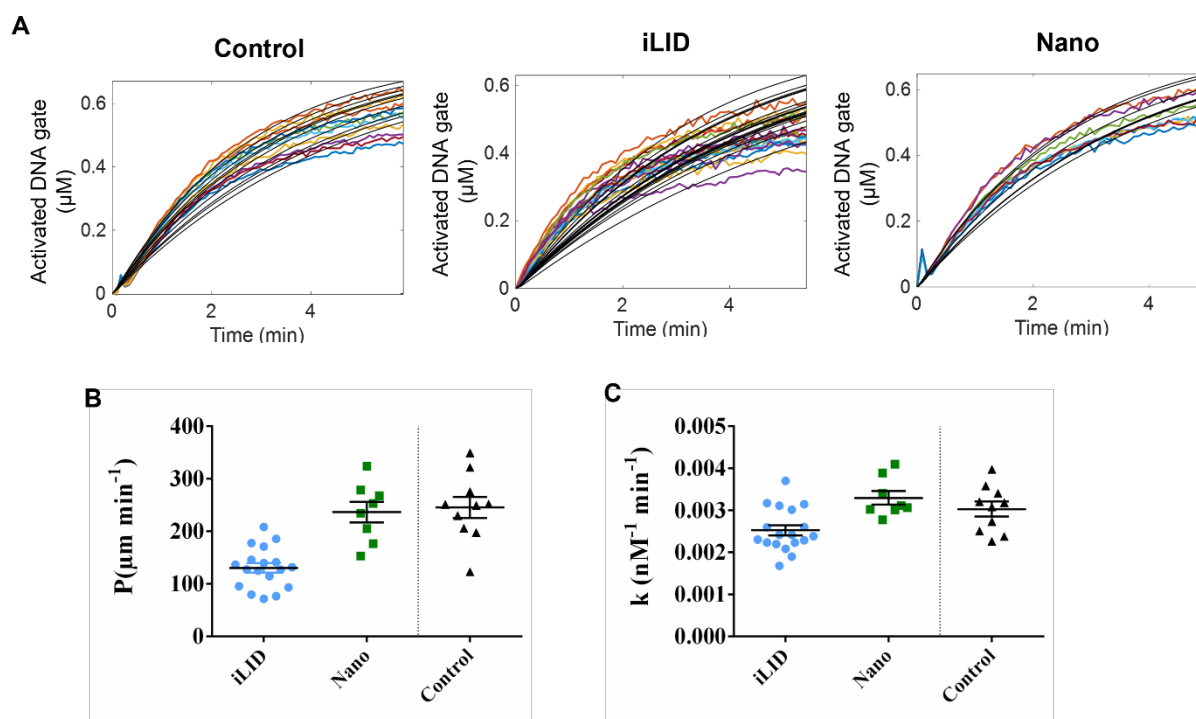


**Figure S12. Effect of protein-functionalization on proteinosome permeability and bimolecular rate constants.** A) Fluorescence measurements (colored traces) and model fittings (black traces) of DSD reactions in proteinosomes functionalized with iLID or Nano protein vs. non-functionalized proteinosomes (control). Reactions were carried out with 100 nM of input (A) strand and to maintain a constant ssDNA concentration in the medium, the input strand solution was slowly flowed through the microfluidic chamber at a rate of approximately  $0.1 \mu\text{l min}^{-1}$  throughout the experiment (see Methods). Concentrations of the activated DNA complex (F:A complex) were determined from time-dependent fluorescence measurements on individual protocells trapped within the microfluidic array device. B) Estimated permeability constants for the different proteinosomes. C) Estimated bimolecular rate constants for the DSD reactions inside the proteinosomes compared to the estimated rate constant for a reference DSD reaction under batch conditions as a control.<sup>[8]</sup> Overall, the results demonstrate that the protein functionalization does not affect the DSD reaction and permeability of the proteinosomes significantly.

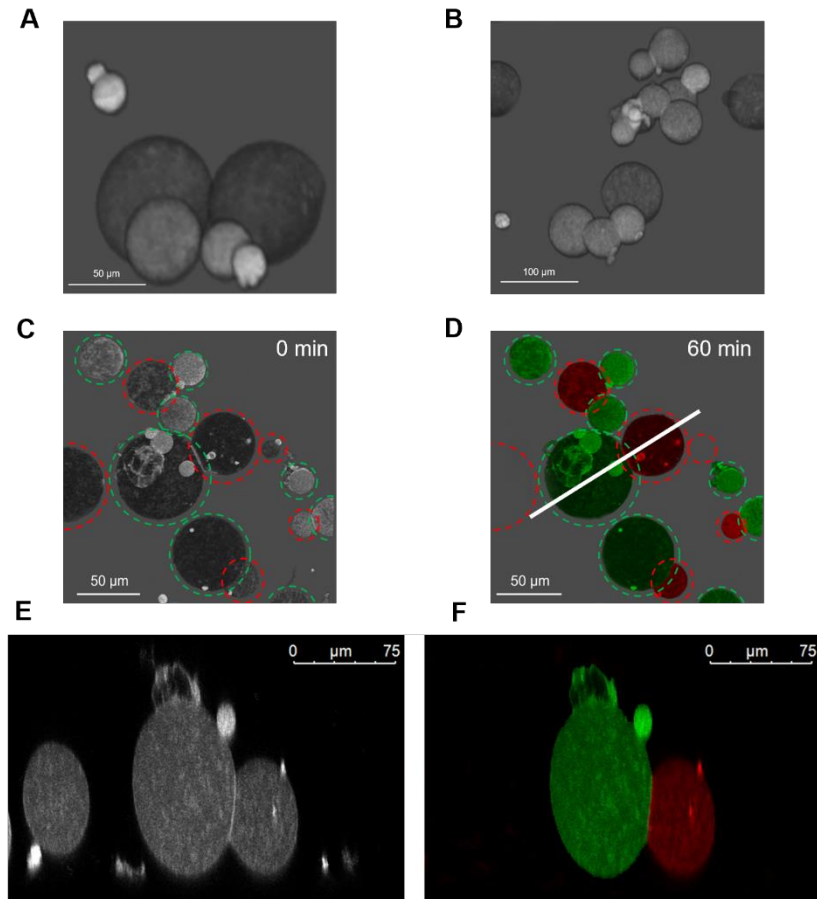


**Figure S13. Contact sites between S and R1-type proteinosomes.** A) 3D images of aggregated S and R1-type proteinosomes in the Rhod B channel after 90 min red light illumination. B) Aggregates of S and R1-type microcapsules after 90 min red light illumination and subsequently triggered DSD reaction. Alexa488 fluorescence in activated S proteinosomes is shown in green, Cy5 fluorescence of activated R proteinosomes is shown in red. Side view of C) Rhod B channel and D) Alexa488 and Cy5 channels across the white line are shown in (E) and (F), respectively. The images show large contact areas between the S and R1-type proteinosomes and membrane deformation due to the PhyB-PIF6 binding under red light.

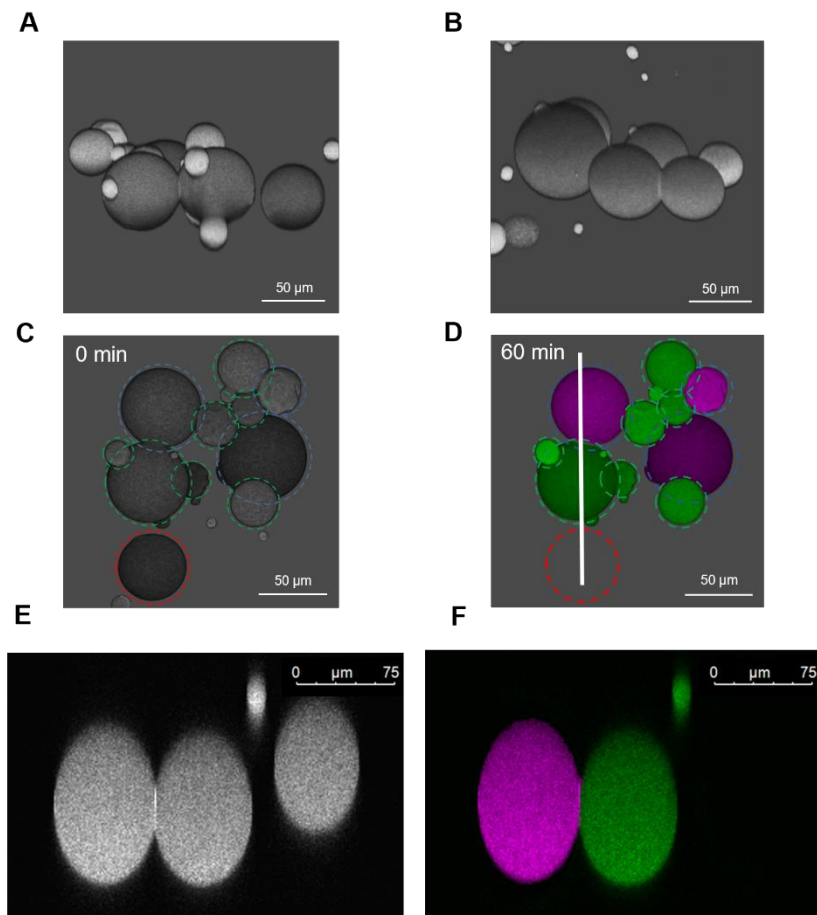
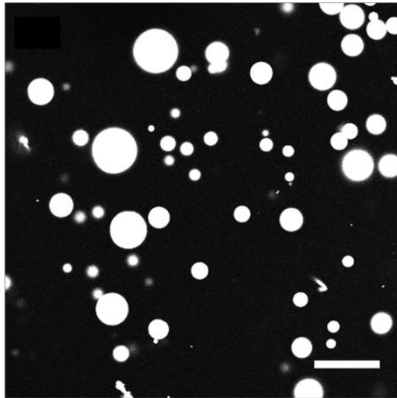


**Figure S14. Contact sites between S and R2-type proteinosomes.** A) 3D images of aggregated S and R2-type proteinosomes in the Rhod B channel after 90 min blue light illumination. B) Aggregates of S and R2-type microcapsules after 90 min blue light illumination and subsequently triggered DSD reaction. Alexa 488 fluorescence in activated S proteinosomes is shown in green, Cy5 fluorescence of activated R proteinosomes is shown in blue. Side view of C) Rhod B channel and D) Alexa488 and Cy5 + Atto425 channels across the white line are shown in (E) and (F), respectively. The images show large contact areas between the S and R2-type proteinosomes and membrane deformation due to the iLID-Nano binding under blue light.



A



B

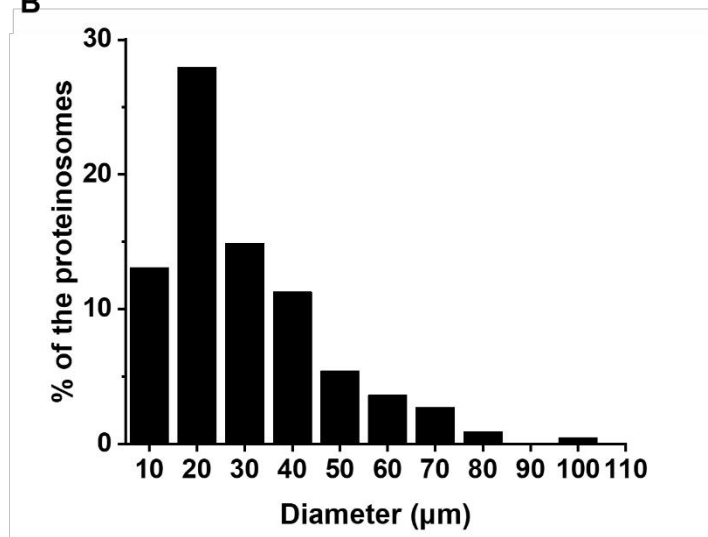


**Figure S15. Size distribution of the proteinosomes.** A) Confocal fluorescence images of proteinosomes in the Rhod B channel. The scale bar is 50 µm. B) Typical size distribution of proteinosomes.  $n > 200$ .

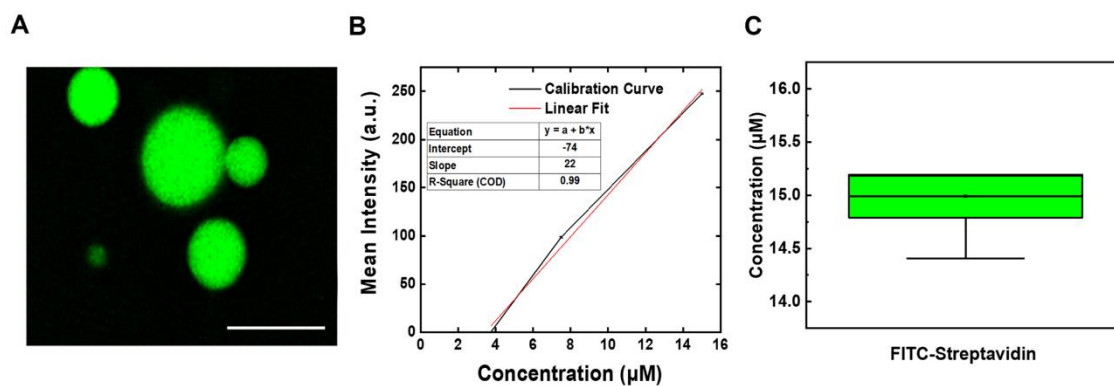


**Figure S16. Encapsulation of the FITC-streptavidin in proteinosomes.** A) Confocal fluorescence microscopy images of the proteinosomes in the FITC channel. The scale bar is 50  $\mu\text{m}$ . B) Standardization curve for FITC-streptavidin at different concentrations. C) Calculated concentration of FITC-streptavidin encapsulated inside the proteinosomes. Error bar is mean  $\pm$  SD ( $n = 3$ ).

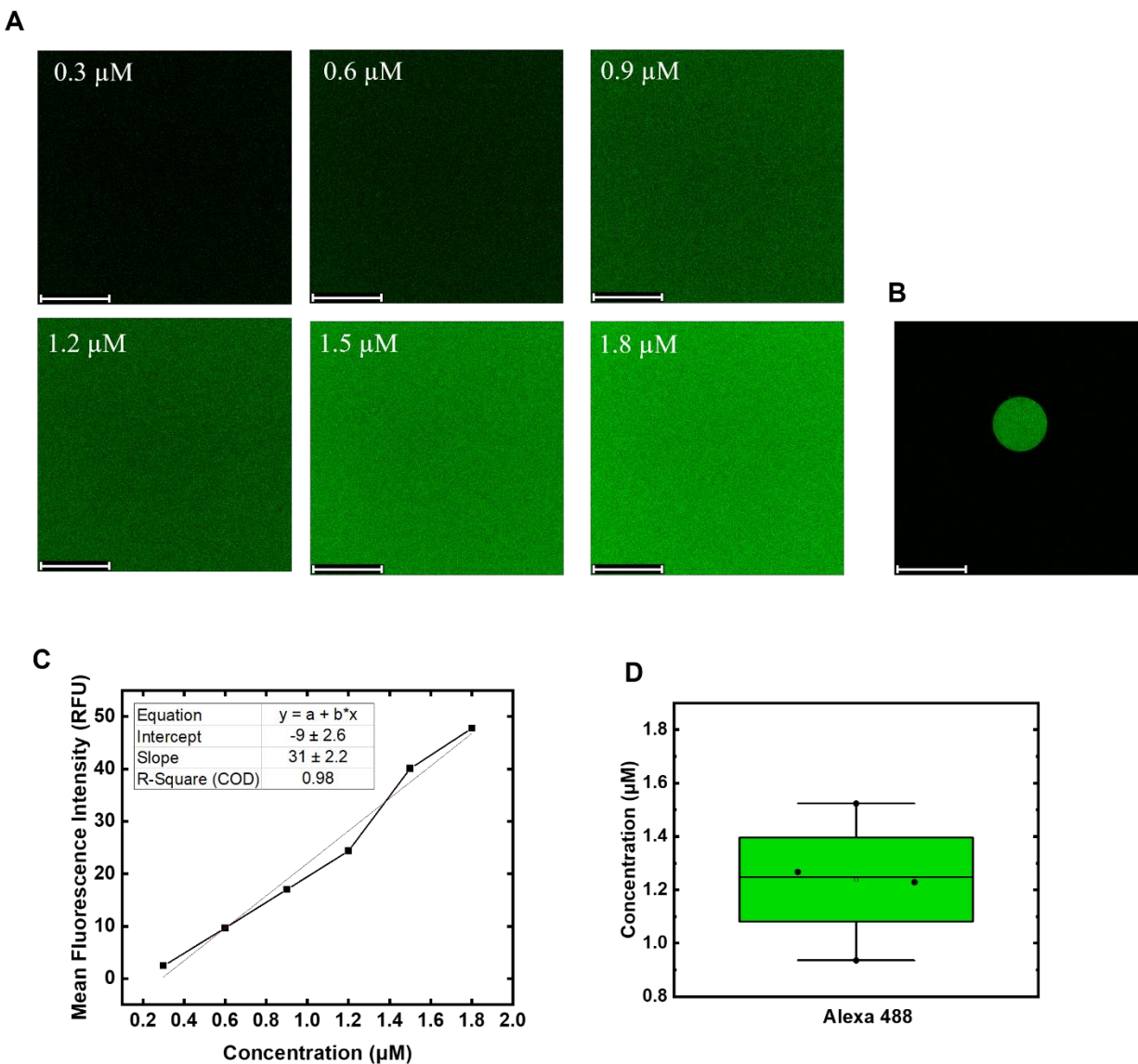


**Figure S17. DNA gate concentration in sender proteinosomes.** A) Confocal fluorescence microscopy images of Alexa488 DNA strand at different concentration in a bulk solution and B) encapsulated inside the sender proteinosomes. The scale bar is 50  $\mu\text{m}$ . B) Standardization curve for Alexa488 DNA gate at different concentrations. C) Calculated concentration of F1:A DNA gate encapsulated inside the proteinosomes. Error bar is mean  $\pm$  SD ( $n = 4$ ).

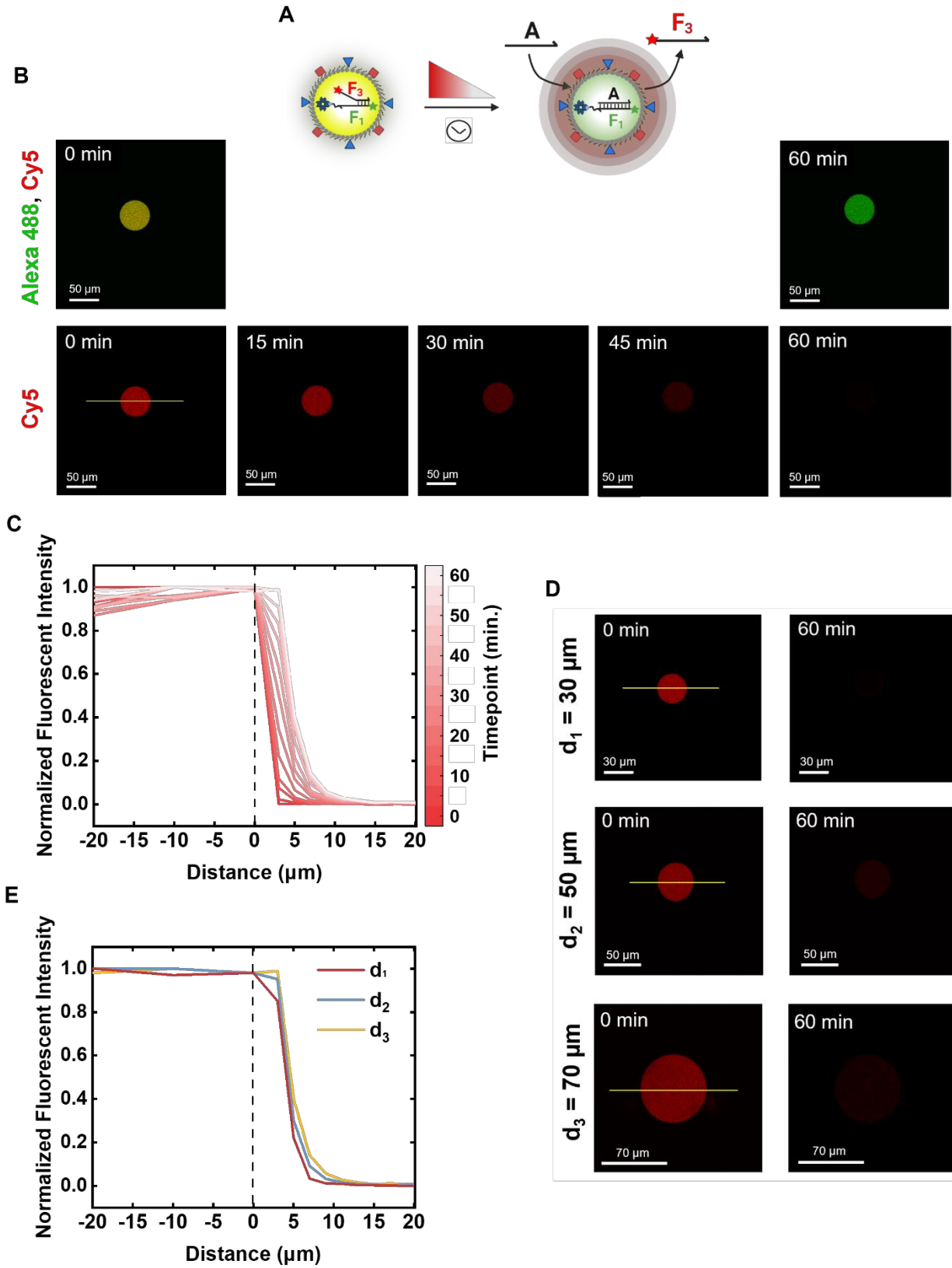


**Figure S18. Signal propagation from sender proteinosome.** A) Upon addition of Input *A* strand the F3 strand with a Cy5 label is released from **S** and diffuses from the sender into the bulk over time. B) Confocal fluorescence microscopy images of the **S** proteinosome after initiating the DSD reaction. C) Fluorescent intensity of F3 strand in **S** plotted for different times as a function of distance across the yellow line. D) Confocal fluorescence microscopy images of **S** proteinosomes with different diameters. E) Fluorescent intensity of F3 strand in **S** plotted as a function of distance across the yellow line after 60 min of DSD reaction initiation. Dash line on the graph represents the periphery of the proteinosome. The fluorescence intensity of each protocell at 1 min intervals was obtained and the average of each distance was plotted for these time points (see methods). n=3

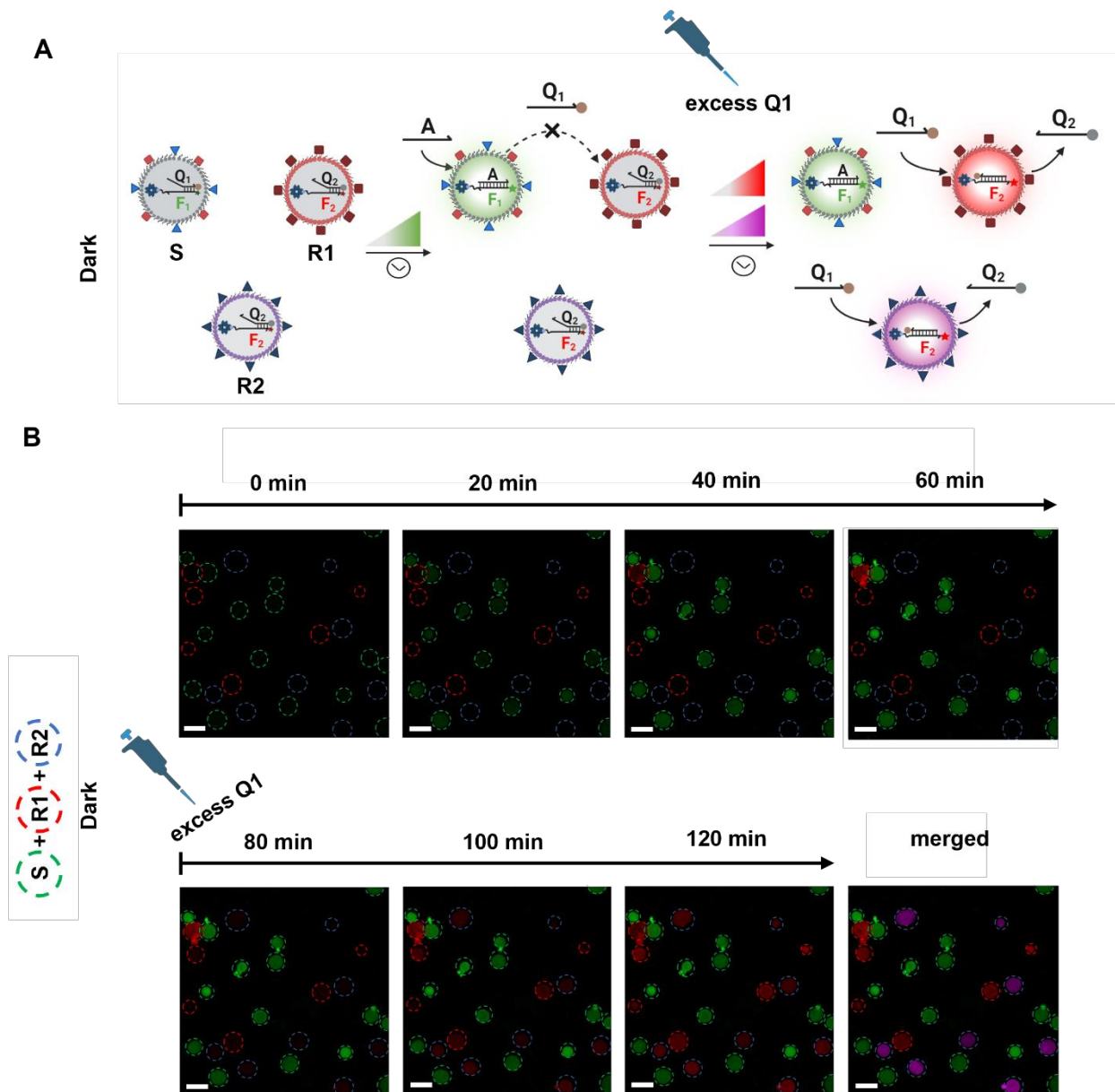


**Figure S19. Activation of all receiver proteinosomes through the addition of external excess Q1 strand.** A) In the dark, R1 and R2 proteinosomes are not in proximity of the S proteinosomes and the Q1 strand released from S proteinosomes can't reach the R proteinosomes. The subsequent external addition of excess Q1 strand activates Cy5 fluorescence both in the R1 and R2 populations. B) Confocal fluorescence microscopy images of 3-membered communities (S:R1:R2 ratio is 2:1:1) after initiating the DSD reaction. Excess Q1 strand (1.0  $\mu$ M) was added after 60 min. Alexa488 fluorescence in activated S proteinosomes is shown in green, Cy5 fluorescence of activated R proteinosomes is shown in red, Atto425 of R2 proteinosomes shown in blue in the merged image. The Cy5 fluorescence in R1 and R2 proteinosomes remained low even after activation of the S proteinosomes but increased both in R1 and R2 proteinosomes after the addition of excess Q1 strand, showing that they were functional. Scale bars are 50  $\mu$ m.